



**Arab American University  
Faculty of Graduate Studies**

**Growth and Characterization of BaSb<sub>2</sub> Alloys**

By  
**Sarah Hakam (Mohammad Ramez) Najar**

Supervisor  
**Prof. Dr. Atef Qasrawi**

**This thesis was submitted in partial fulfillment of the  
requirements for the Master's degree in Physics**

**June /2020**

**© Arab American University - 2020.  
All rights reserved.**

## **Growth and Characterization of BaSb<sub>2</sub> Alloys**

**By**

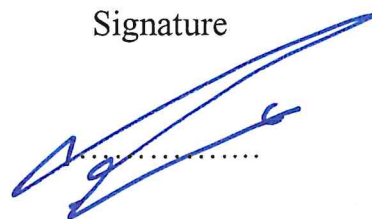
**Sarah Hakam (Mohammad Ramez) Najar**

This thesis was defended successfully in June 10<sup>th</sup> 2020 and approved by:

Committee members

Signature

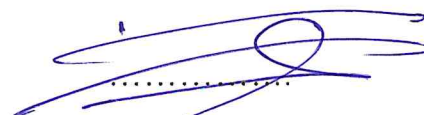
1. Prof. Dr. Atef Fayez Qasrawi ( Supervisor)



2. Assoc. Prof. Dr. Ahmad Yousef Omar (Internal examiner) .....



3. Prof. Dr. Ghassan Saffarini (External examiner)



## **Declaration**

The work in this thesis, unless otherwise referenced, is the researcher's own work and has not been submitted elsewhere for any other degree or qualification.

Student's Name: **Sarah Hakam (Mohammad Ramez) Najar**

## **Acknowledgments**

There are many roads I walked within them which brought me to the point that I am standing in it now, all roads started with my family to schools to the Arab American university were under the care of Allah absolutely. I am very grateful to all who helped me through all that steps of my life. To whom taught me any letter, any number, any information, any advice, any frustration which made me stronger to continue my war in learning.

The list is too long and the things that brought me to this step of my life are really much. So Proceeding from that I would like to thank my parents and all the teaching staff along my life till today especially noteworthy my supervisor Prof. Dr. Atef Qasrawi , the science and research assistant Ms Olfat Abdulfatah Omareya and my partner in the lab Ms Shadia Elayyat .



## Abstract

In this thesis, BaSb<sub>2</sub> alloys are produced and characterised. The alloys which are prepared by the melting of the Ba and Sb in stoichiometric compositions in a vacuum of 10<sup>-5</sup> mbar at 735 °C are structurally and electrically investigated. Deep structural investigations with the help of x-ray diffraction, " Crystdiff ", " Treor 92" and " phywe measure 4 " software packages has shown that the alloys are composed of monoclinic structure (58.46%) and other minor phases (41.54%). The structural parameters indicated that the alloys are composed of nano crystallites and exhibit low percentage of stacking faults and low defect density. The morphology analysis which were carried out with scanning electron microscopy have shown that the alloys are of layered types and contains narrow cracks of lengths of 5.0 µm. Electrically, the alloys are metal like p-type materials which exhibit temporary metal-insulator transitions at low temperatures. The AC analysis on the capacitance and conductance spectra which were measured in the frequency domain of (0.01-1.8) GHz have shown that the capacitance exhibits negative capacitance effect owing to the injection of holes being larger than electrons. In addition, modelling of the conductance spectra in the main frequency domain has shown that the BaSb<sub>2</sub> alloys are dominated by the correlated barrier hopping conduction at scattering times of picosecond scales . The electrical properties of the BaSb<sub>2</sub> alloys nominate them for use in circuits as parasitic capacitance cancellers ,as noise reducers and as microwave cavities .

## List of contents

	Title	Page No.
	List of tables	vii
	List of figures	viii
Chapter One	<b>Introduction</b>	
	1.1 Application of alloys and their classification.	1
	1.2 Alloys' preparation methods and their characterization.	2
	1.3: Properties of Barium and Antimony metals..	2
Chapter Two	<b>Theoretical Background</b>	
	2.1 X-ray analysis.	5
	2.2 Impedance spectroscopy.	8
	2.2.1: RLC circuit in series.	8
	2.2.2: RLC circuit in parallel.	10
	2.3: Alternating current conduction mechanisms in solids.	12
	2.4: Alternating current capacitance mechanisms in solids.	14
	2.5: Temperature effect on metal insulator transitions.	17
Chapter Three	<b>Experimental Details</b>	
	3.1 Alloys formation.	19
	3.2 X-ray diffraction (XRD).	22
	3.3 Scanning electron microscopy (SEM).	23
	3.4 Impedance spectroscopy measurements.	25
	3.5 Current-Voltage (IV) Measurements.	26
Chapter Four	<b>Results and Discussion</b>	
	4.1 XRD results.	28

	4.2 Scanning electron microscopy results.	39
	4.3 Impedance Spectroscopy.	46
	4.4 I-V Characteristics.	53
Chapter Five	<b>Conclusions</b>	55
References		56
المخلص		62

---

### List of tables

No	Title	Page No
2.1	The six crystal structures systems, their properties and obtained interplanner distance.	6
4.1	The “Crysdiff” software data that include the theoretical values of $2\theta$ the associated diff % for Ba, Sb, BaSb <sub>2</sub> , BaSb <sub>3</sub> , Sb <sub>2</sub> O <sub>3</sub> and BaO.	33
4.2	The “Crysdiff” software data include only the diff % values to obvious view for the differences between the experimental $2\theta$ and the calculated or theoretical ones.	34
4.3	Data was given by “TREOR 92” software shows the entered experimental $2\theta$ , their associated intensity and what the diff % for each expected structure.	35
4.4	Data obtained from " phywe measure 4 " software.	36
4.5	The calculated lattice parameters of the prepared BaSb <sub>2</sub> alloys and the theoretical parameters of the mixing metals Ba and Sb.	37
4.6	The structural parameters of monoclinic phase of BaSb <sub>2</sub> alloys.	39
4.7	The fitting parameters of the capacitance and conductance of BaSb <sub>2</sub> alloys.	49

## List of figures

No	Caption	Page No
2.1	The series RLC circuit..	9
2.2	Phasor diagram for a Series RLC circuit.	10
2.3	The parallel RLC circuit.	10
2.4	Phasor diagram for a parallel RLC circuit.	11
3.1	The illustration of the quartz boat in the evaporation source. (item 1 for Shutter ,item 2 for quartz boat , item 3 for thermocouple ) .	19
3.2	Evaporation source.	21
3.3	The Rigaku Miniflex 600 diffractometer.	23
3.4	The illustration of the SEM.	24
3.5	Impedance analyser.	25
3.6	The prepared BaSb <sub>2</sub> bulk sample for the IV measurement.	26
3.7	IV measurements	27
4.1	The XRD patterns for BaSb <sub>2</sub> alloys.	28
4.2	The three layers of the BaSb <sub>2</sub> bulk at 100 amplification.	39
4.3	The top layer of the BaSb <sub>2</sub> bulk at different amplifications (500, 1000,5000,10000) for a, b, c and d respectively.	40
4.4	The second layer of the BaSb <sub>2</sub> bulk at different amplifications (1000, 5000, 10000) for a, b and c respectively.	42
4.5	The third layer of the BaSb <sub>2</sub> bulk at different amplifications nearly (500, 5000 and 10000) for a, b and c respectively.	44
4.6	Modeling of the experimental capacitance (the red line) with the theoretical or calculated one (the blue line).	47
4.7	The conductance spectra for the BaSb <sub>2</sub> bulk in the frequency range (0.01-1.8) GHz.	49
4.8	ln(G) versus ln(w) for a part of data to show the fitted line of their graph .	50
4.9	Modeling of the experimental conductance (the red line) with the theoretical or calculated one (the blue line).	51
4.10	The impedance spectra for the BaSb <sub>2</sub> bulk in the frequency range (0.01-1.8)GHz.	52

4.11	The current voltage characteristics of BaSb <sub>2</sub> alloys.	53
4.12	The resistivity-temperature variations of the BaSb <sub>2</sub> bulk.	54

---

## Chapter One

### Introduction

#### 1.1 : Application of alloys and their classification.

Metallic alloys capture the focus of research centers owing to its wide range of applications in electronics and optoelectronics. Thermocouple alloys have found a wide-range of use in temperature sensing and control such as thermocouple made of Pt-Rh alloys [1]. Some alloys like Magnesium alloys have promising applications in aerospace, automotive, and 3C (Computer, Communication and Customer Electronic) industries due to its engineering properties such as high thermal conductivity, electromagnetic compatibility, easy recycling and high specific rigidity [2]. FeCoCrNi high-entropy alloy is found to be as an input material for selective laser melting [3]. Aluminum alloys are used for high performance applications including automobile parts [4]. Aluminum-silicon (Al Si) alloys are widely used in many industrial applications such as automotive and aircraft industries due to its light weight, cheapness, low density, good appearance, high thermal and electrical conductivity [5]. Alloys are also employed as shape memories which are used as actuators and sensors [6]. Co–W alloys are found to be good materials as catalysts beneficial for Li–O<sub>2</sub> battery's electrodes [7].

Alloys are classified in several ways. Based on the presence or absence of iron. Alloys can be classified into ferrous alloys which contain iron as a major component and non-ferrous alloys which does not contain iron as a major component [8]. Substances sources of ferrous alloys are stainless steel, cobalt, gallium, silver, gold, bismuth, and zirconium. Aluminum, brass, bronze, copper, tin, nickel, magnesium, and titanium are some common substances sources non-ferrous alloys. Based on their structure features one or more of the following phases may exist: solid solution, intermediate phases, and phase mixtures

depending on the types of the metals present in the alloy [8]. In regard with the base metal, alloys could be classified as Aluminum alloys, Magnesium alloys, Titanium alloys and Copper alloys [8].

### **1.2: Alloys' preparation methods and their characterization.**

Many methods could be used to prepare an alloy such as the fusion method which uses alloying elements in a fixed proportion and fuses them together [9], pulsed electro-deposition method [10], the reduction method [11] and powder metallurgy [12]. Alternatively, the chemical vapor deposition (CVD) [13], mechanisms of selective laser melted alloy in which the laser scan pattern rotated by an angle with each next layer [14] and additive manufacturing is a layer-by-layer process method are also used to produce alloys [14]. From characterization point of view, when choosing the elements of the alloy, the chemical, physical, mechanical, biocompatibility and technological characteristics must be taken into account [15]. Scanning electron microscopy (SEM) and X-ray diffraction technique (XRD) could be used to understand the morphology and structure of the alloys, respectively.

### **1.3: Properties of Barium and Antimony metals.**

As a material which is remarkable of interest, we are considering the Barium (Ba) element as a candidate of forming an alloy. Barium is a soft, silvery white metal. Classified as an alkaline earth metal. Its atomic weight (average mass of the atom) 137.327 g/mol. It has a body centered cubic (bcc) structure [16] and a lattice constants of 5.028 Å. Barium is found naturally only in combination with other elements because of its high level of reactivity. Barium does not have many practical uses, due to reason assigned previously. However, the strong attraction of Ba to oxygen makes it useful as a "getter" to remove



the last traces of air in vacuum tubes [17]. Pure Ba can be also combined with other metals to form alloys that are used to produce machine elements such as bearings or spark plugs in internal combustion engines. Ba alloys emit electrons easily when heated because barium has a loose hold on its electrons and this improves the efficiency of the spark plugs [18]. Ba–Al and Ba–Mg or ternary alloys Ba–Mg–Na can find application in Microelectromechanical systems (MEMS) [18].

On the other hand, Antimony (Sb) is also another material that is worth of consideration. Sb is an extremely brittle metal of a flaky, crystalline texture. It is bluish white and has a metallic luster with atomic weight of 121.76 g/mol. It has a simple trigonal structure [19] with lattice parameters ( $a=4.307$ ,  $b=4.307$ ,  $c=11.273$ ) Å and  $\gamma=120$ . It is not reacted with air at room temperature, but burns when is heated with the formation of white fumes. It is a poor conductor of heat and electricity. It is mostly used today for various applications such as fire retardants [20] and ball bearings [21]. Sb has recently found applications in semiconductors and microelectronics. Aluminum antimony alloy was explored as an anode material for lithium-ion and sodium-ion batteries [22]. Aluminum bismuth antimony ternary alloys were recently found to be suitable for optical telecommunication applications [23]. Lead antimony alloys containing 0.2 to 1 wt % Sb are used to make barrier sheaths in high voltage cables [24]. GaSb thin films are also used for application in phase change memories [25]. Sn–Ge–Sb thin film alloys are used for application in sodium ion batteries due to their high theoretical capacity and suitable operating voltage [26].

In this work, we will construct new class of Ba-Sb alloys for the purpose of use in electronics and microwave technology. The results of the alloying on the performance of

the microwave traps will be stated clearly. The relation between the structural parameters and the electronic performance is established and connected to theories.

The thesis discusses the theoretical background of the used techniques in the second chapter. The experimental investigations and procedures that are employed to prepare the alloys, are also considered in the third chapter. The fourth chapter will discuss the most important results about the preparation procedure, the formed alloy's structure and the electrical performance of the alloy. Concluding remarks are considered in chapter five.

## Chapter Two

### Theoretical Background

#### 2.1: X-ray analysis

Crystals could have one or many of the structural phases. In general, there are seven crystal systems named triclinic, monoclinic, orthorhombic, tetragonal, cubic, hexagonal and trigonal. These systems can be defined in terms of the relationships between lattice vectors  $(a, b, c)$  and lattice angles  $(\alpha, \beta, \gamma)$  [27]. Each system has an interplanar distance or spacing ( $d$ ). This quantity is the perpendicular distance between two successive planes on a family of miller indices  $(hkl)$ . We will start with the triclinic formula in order to reach other structural formulas. In this system, there is no relationships between the lattice parameters:  $(a \neq b \neq c)$  and lattice angles  $(\alpha \neq \beta \neq \gamma \neq 90^\circ)$ .

$$\frac{1}{d^2} = \frac{\left[ \frac{h^2}{a^2} \sin^2 \alpha + \frac{k^2}{b^2} \sin^2 \beta + \frac{l^2}{c^2} \sin^2 \gamma + \frac{2kl}{bc} (\cos \beta \cos \gamma - \cos \alpha) + \frac{2hl}{ac} (\cos \alpha \cos \gamma - \cos \beta) + \frac{2hk}{ab} (\cos \alpha \cos \beta - \cos \gamma) \right]}{[1 - \cos^2 \alpha - \cos^2 \beta - \cos^2 \gamma + 2 \cos \alpha \cos \beta \cos \gamma]} \quad (2.1)$$

Using equation 2.1 one may derive all the other structural phases. These important phases are shown in table 2.1.

Table 2.1: The six crystal structures systems, their properties and obtained interplanner distance.

Crystal system	lattice constant and angles	Interplanner distance formula	
Monoclinic	$a \neq b \neq c, \alpha = \gamma = 90^\circ \neq \beta$	$\frac{1}{d^2} = \frac{1}{\sin^2 \beta} \left[ \frac{h^2}{a^2} + \frac{k^2 \sin^2 \beta}{b^2} + \frac{l^2}{c^2} - \frac{2 hl \cos \beta}{ac} \right]$	(2.2)
Orthorhombic	$a \neq b \neq c, \alpha = \beta = \gamma = 90^\circ$	$\frac{1}{d^2} = \frac{h^2}{a^2} + \frac{k^2}{b^2} + \frac{l^2}{c^2}$	(2.3)
Tetragonal	$a = b \neq c, \alpha = \beta = \gamma = 90^\circ$	$\frac{1}{d^2} = \left[ \frac{h^2 + k^2}{a^2} \right] + \frac{l^2}{c^2}$	(2.4)
Cubic	$a = b = c, \alpha = \beta = \gamma = 90^\circ$	$\frac{1}{d^2} = \frac{h^2 + k^2 + l^2}{a^2}$	(2.5)
Hexagonal	$a = b \neq c, \alpha = \beta = 90^\circ, \gamma = 120^\circ$	$\frac{1}{d^2} = \frac{4}{3} \left[ \frac{h^2 + k^2 + hk}{a^2} \right] + \frac{l^2}{c^2}$	(2.6)
Trigonal	$a = b = c, \alpha = \beta = \gamma \neq 90^\circ$	$\frac{1}{d^2} = \frac{[(h^2 + k^2 + l^2) \sin^2 \alpha + 2(hk + kl + lh)(\cos^2 \alpha - \cos \alpha)]}{a^2(1 - 3 \cos^2 \alpha + 2 \cos^3 \alpha)}$	(2.7)

From table 2.1 the lattice constant ( $a, b, c$ ) and the lattice angles ( $\alpha, \beta, \gamma$ ) of the other systems are substituted in the triclinic equation (2.1) to obtained the interplanner formulas (2.2-2.7).

X-ray diffraction (XRD) is a technique for characterizing crystalline materials. These rays are generated by a cathode ray tube, filtered to produce monochromatic radiation, collimated to concentrate the rays, and then directed toward the sample [28]. It provides information about the structures, phases, crystal orientations and other structural parameters, such as interplanner distance ( $d$ ), average grain size or crystallite size ( $D$ ), stacking faults percent ( $SF\%$ ), dislocation density ( $\delta$ ) along a line and strain ( $\epsilon$ ) from the broadening width ( $\beta$ ) of all observed peaks using will known relations [29]. XRD peaks are produced by constructive interference of a collimated monochromatic beam of X-rays scattered at specific angles from a set of parallel lattice planes in a sample. Interplanner distance ( $d$ ) is calculated from Bragg equation [30]:

$$2 d \sin\theta = n\lambda \quad (2.8)$$

Where  $n$  is an integer (order of reflection),  $\lambda$  is the wavelength of incident X-rays in our case  $\lambda = 1.5405 \text{ \AA}$ ,  $d$  is the interplanner distance between successive atomic planes, and  $\theta$  is the angle of incidence or the angle of reflection. The other structural parameters ( $D, \epsilon$ ) could be found using Scherrer equation which connects the crystallites grain size with the broadening of a diffraction peak.

$$\beta \cos\theta = \frac{K\lambda}{D} + 4\epsilon \sin\theta \quad (2.9)$$

Where  $D$  as we defined is the size of the crystallites,  $\beta$  is width at half maximum intensity of peaks in radians,  $K$  is a constant related to crystallite shape, taken as 0.94 [30]  $\theta$  is the

incidence angle in rad and  $\varepsilon$  is the strain. Equation (2.9) has limitation presented on the grain size value which indicates the validity of this equation only below 200 nm.

Stacking faults represents a local error in the order of the sequential layering of crystallographic planes or a type of defect that characterizes the disordering of that planes and is given by equation (2.10).

$$SF\% = \frac{2\beta \pi^2}{45\sqrt{3}\tan\theta} \times 100\% \quad (2.10)$$

In general, the word dislocation means a defect or irregularity. The existence of this quantity influences many of the properties of materials. Dislocation density ( $\delta$ ) is the total length of dislocation lines per unit area and can be calculated from relations used [31-32]:

$$\delta = \frac{15\varepsilon}{aD} \quad \text{lines/cm}^2 \quad (2.11)$$

Where  $\varepsilon$  is the strain,  $a$  is the lattice constant and  $D$  is the crystallite size.

## 2.2: Impedance spectroscopy

The name of the RLC circuit is derived from the letters that are used to denote the components of this circuit. It is an electrical circuit consisting of a resistor (R), capacitor (C) and inductor (L) connected in series or in parallel.

### 2.2.1: RLC circuit in series

The series RLC circuit has a single loop with the instantaneous current flowing through it and have the same value for each circuit element. The source voltage  $V_s$  drops across circuit component  $R$ ,  $L$  and  $C$  with  $V_R$ ,  $V_L$  and  $V_C$  values, respectively. These voltages will be out of phase with each other's [33]. While  $V_R$  is in-phase with current,  $V_L$  leads the

current by  $90^\circ$  and  $V_C$  lags the current by  $90^\circ$ . Thus,  $V_L$  and  $V_C$  are  $180^\circ$  out of phase and in opposition to each other [33]. (See figure 2.1)

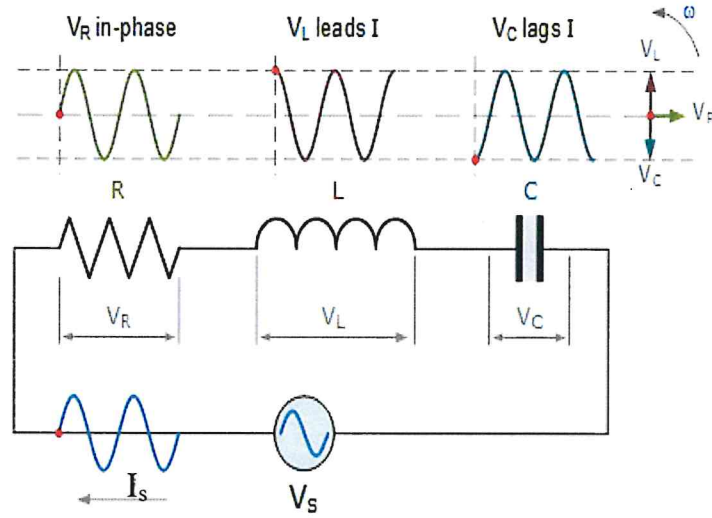


Fig 2.1: The series RLC circuit.

According with Kirchhoff's voltage law [34], the instantaneous voltages for a series RLC circuit is obtained as below,

$$V_S - V_R - V_L - V_C = 0 \quad (2.12)$$

$$V_S - IR - L \frac{dI}{dt} - \frac{Q}{C} = 0 \quad (2.13)$$

$$V_S = IR + L \frac{dI}{dt} + \frac{Q}{C} \quad (2.14)$$

But the voltage triangle for a series RLC circuit results in.

$$V_S = \sqrt{V_R^2 + (V_L - V_C)^2} = I \cdot \sqrt{R^2 + (X_L - X_C)^2} = I \cdot Z \quad (2.15)$$

where  $I$  the current  $X_L$  inductive reactance  $X_C$  capacitive reactance and  $Z$  the impedance.

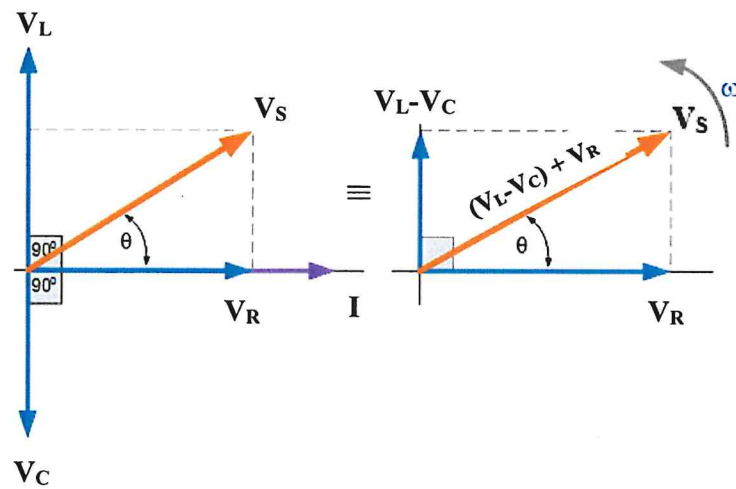


Fig 2.2: Phasor diagram for a series RLC circuit.

### 2.2.2: RLC circuit in parallel

In this connection type, the applied voltage is common to all components of the RLC circuit instead of the current so we need to find the individual currents through each element, current through  $R$  ( $I_R$ ), current through  $L$  ( $I_L$ ) and current through  $C$  ( $I_C$ ). The circuit is shown in figure 2.3.

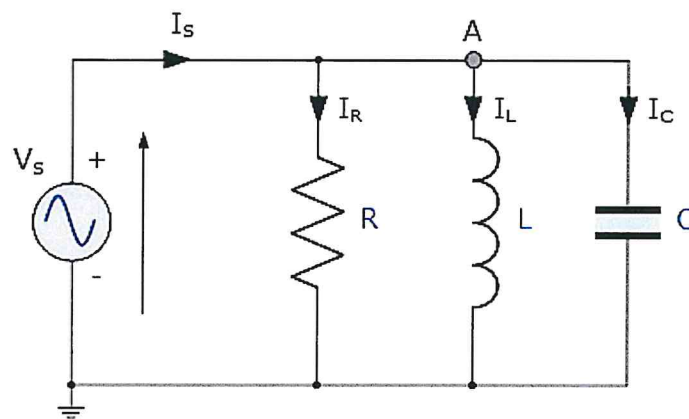


Fig 2.3: The parallel RLC circuit.



The current flowing through each branch will not necessarily be equal to each other. Therefore, each component will be mostly different to each other and to the supply current ( $I_S$ ). The total current drawn from the supply will not be the mathematical sum of the three individual branch currents but their vector sum [33]. Again through each branch the current is found using Kirchoff's current law [33] :

$$I_S = I_R + I_L + I_C \quad (2.16)$$

$$I_S = \frac{1}{RC} \frac{dV}{dt} + \frac{V}{LC} + C \frac{d^2V}{dt^2} \quad (2.17)$$

but the current Triangle for a parallel RLC Circuit resulted in:

$$I_S = \sqrt{I_R^2 + (I_L - I_C)^2} = \sqrt{\left(\frac{V}{R}\right)^2 + \left(\frac{V}{X_L} - \frac{V}{X_C}\right)^2} = \frac{V}{Z} \quad (2.18)$$

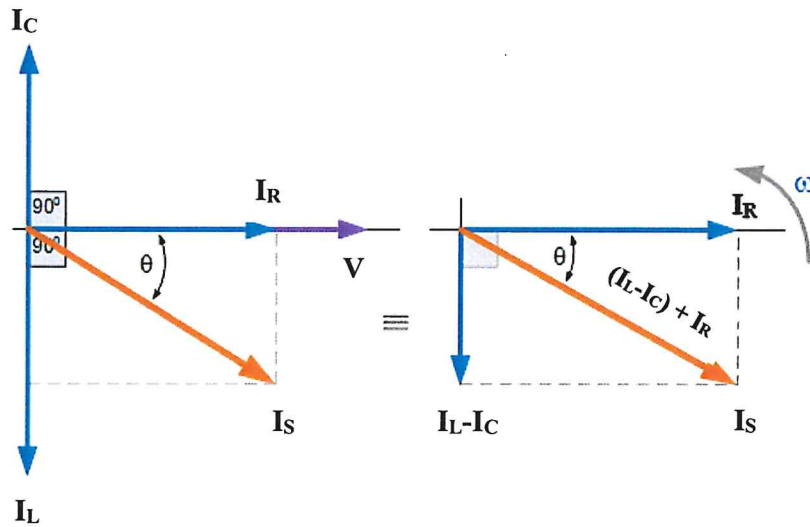


Fig 2.4: Phasor Diagram for a parallel RLC Circuit.

### 2.3: Alternating current conduction mechanisms in solids.

The alternating current (AC) conductivity spectra could be referred to the quantum mechanical tunnelling (QMT) or correlated barrier hopping conduction (CBH) or may be both [35]. Conductivity could be obtained from the conductance ( $G$ ) according to the following relation:

$$G = \sigma * \frac{A}{l} \quad (2.19)$$

Where  $G$  is the measured conductance,  $\sigma$  is the conductivity,  $A$  is the cross sectional area and  $l$  is the length of the conductor. Early published theories [36-37] assume that the conductivity is a function of frequency and follows the relation,

$$\sigma(w) = Aw^s \quad (2.20)$$

Where  $A$  is a constant dependent on temperature,  $w$  is the frequency and  $s$  is the exponent that is generally less than or equal to unity. This shape of the conductivity equation (2.20) appears if the mechanism of loss has a wide range of relaxation times ( $\tau$ ). The exponent value  $s = 1$  is founded if the distribution of relaxation times ( $n(\tau)$ ) is inversely proportional to  $\tau$ . In that case, the relaxation time ( $\tau$ ) is given by the equation:

$$\tau = \tau_0 e^\xi, \quad (2.21)$$

where  $\xi$  is a random variable.

In the case where QMT dominates  $\xi = 2\alpha R$  with  $R$  referring to the intersite separation and  $\alpha$  is spatial decay parameter of the wave functions that is employed to describe the localized state at each site.  $\alpha$  is nearly constant for all sites and equal  $0.1 \text{ \AA}^{-1}$  [36]. For an electron undergoing quantum mechanical tunnelling, the AC conductivity is given by the equation [37],

$$\sigma_{QMT}(w) = \frac{\pi^4 e^2 K T \alpha^{-1} (N(E_F))^2 w R_w^2}{24} \quad (2.22)$$

In this equation,  $N(E_F)$  is the density of states near the Fermi level (assumed constant with varying frequency) and  $R_w$  is the hopping distance at a particular frequency  $w$ .  $R_w$  is given by,

$$R_w = \frac{1}{2\alpha} \ln \left( \frac{1}{w\tau_o} \right) \quad (2.23)$$

The frequency dependence of  $\sigma(w)$  in the equation (2.20) can be used to execute the derivative  $s$ . Taking the logarithm for both sides of equation (2.20) becomes:

$$\ln \sigma(w) = \ln A + s \ln(w). \quad (2.24)$$

Executing the derivative for each side,

$$d \ln \sigma(w) = 0 + s d \ln(w) \quad (2.25)$$

From equation (2.25) we conclude that the exponent  $s$  can be found from the relation,

$$s = \frac{d \ln \sigma(w)}{d \ln(w)} \quad (2.26)$$

For the QMT model,  $s$  is given by:

$$s = 1 - \frac{4}{\ln(1/w\tau_o)} \quad (2.27)$$

Thus, for the QMT model, the frequency exponent  $s$  is frequency dependent and decreases with increasing frequency at constant temperature. On the other hand, the CBH theory supposes that  $\xi = \frac{W_h}{KT}$  with  $W_h$  being the hopping barrier height, for this case, as long as the frequency of the signal that propagates is less than the charge of the carrier jump frequency, the AC conductivity will increase with that frequency [37]. The AC conductivity for CBH is given by the following relation:

$$\sigma_{CBH}(w) = \sigma_H(w) + \frac{(\sigma_L(w) - \sigma_H(w))}{(1 + w^2 \tau^2)} \quad (2.28)$$

Where, the subscript symbols H and L means conductivity at high and low frequency, respectively. As previously mentioned, it is possible that the AC conductivity refers to the domination of the two conduction mechanisms QMT and CBH,

$$\frac{1}{\sigma_{tot}} = \frac{1}{\sigma_{QMT}} + \frac{1}{\sigma_{CBH}} \quad (2.29)$$

Where,  $\sigma_{tot}$  is the total conductivity,  $\sigma_{QMT}$  is the conductivity resulted from quantum mechanical tunnelling and  $\sigma_{CBH}$  is the conductivity resulted from correlated barrier hopping conduction.

#### 2.4: Alternating current and capacitance mechanisms in solids.

Here we consider Ershov Motel [38] for negative capacitance effect (NC). It illustrates the effect of negative capacitance in terms of time range transient currents in response to a small voltage signals. Ershov supposed that entering step or pulsed voltage will lead to an instantaneous change of charges on the contacts. According to this approach, the total capacitance ( $C(w)$ ) consists of geometric part ( $C_0$ ) and relaxation part ( $C_1$ ) [39].  $C_1$  was found to be due to the impact ionization, electron transport, trapping and other physical process [36]. The theorems of Ershov arrived at the conclusion of Jonscher which state that the source of NC is related to the positive or nonmonotonic behaviour of the derivative of the transient current ( $j(t)$ ) as a response to a small voltage step. Using this approach which is based on the charge nonmonotonic or monotonic variations, Qasrawi et al [36-37] assumes a presence of two different frequency domains ( $w-w_p$ ) and ( $w-w_n$ ) where  $w_p$  and  $w_n$  are the limits of frequency domains in the  $p$  and  $n$  regions, respectively. As a result equation of Ershov which takes the form,

$$C_1 = \frac{\Delta Q}{\Delta V} = \frac{1}{\Delta V} \int_0^\infty \delta_j(t) \cos wt \, dt = \frac{1}{w\Delta V} \int_0^\infty \left( -\frac{d\delta_j(t)}{dt} \right) \sin wt \, dt \quad (2.30)$$

it can be rewritten as:

$$C_1 = \frac{\Delta Q}{\Delta V} = \frac{1}{\Delta V} \int_0^\infty \delta_j(t) \cos(w - w_{n,p})t \, dt \quad (2.31)$$

$$C_1 = \frac{1}{w\Delta V} \int_0^\infty \left( \frac{-d\delta_j(t)}{dt} \right) \sin(w - w_{n,p})t \, dt \quad (2.32)$$

Where  $\Delta Q$  is the charge,  $\Delta V$  is the voltage,  $w_n$  and  $w_p$  as defined previously and  $\delta_j(t)$  is the time domain behaviour of the transient current. If  $\delta_j(t)$  is positive valued and decreases monotonically to Zero as  $t$  goes to  $\infty$  then,  $C_1 > 1$  and  $C(w) > C_0$  at any frequency. Ershov's approach also assumes [38],

$$\delta_j(t) = \Delta V [a_n e^{-t/\tau_n} - a_p e^{-t/\tau_p}] \quad (2.33)$$

Where  $a_n$  and  $a_p$  are parameters in F/s. It represents the rate of change of dynamic capacitance with time

$$\frac{d\delta_j(t)}{dt} = \Delta V \left[ \frac{-a_n}{\tau_n} e^{-t/\tau_n} + \frac{a_p}{\tau_p} e^{-t/\tau_p} \right] \quad (2.34)$$

Substituting 2.34 in 2.32

$$C_1 = \frac{1}{w\Delta V} \int_0^\infty - \left( \Delta V \left[ \frac{-a_n}{\tau_n} e^{-t/\tau_n} + \frac{a_p}{\tau_p} e^{-t/\tau_p} \right] \right) \sin(w - w_{n,p})t \, dt$$

$$C_1 = \frac{1}{w} \int_0^\infty \left( \frac{a_n}{\tau_n} e^{-t/\tau_n} \sin(w - w_n)t \, dt - \frac{a_p}{\tau_p} e^{-t/\tau_p} \sin(w - w_p)t \, dt \right)$$

$$C_1 = \frac{a_n}{w\tau_n} \int_0^\infty e^{-t/\tau_n} \sin(w - w_n)t \, dt - \frac{a_p}{w\tau_p} \int_0^\infty e^{-t/\tau_p} \sin(w - w_p)t \, dt \quad (2.35)$$

By using Fourier integral form

$$\sqrt{\frac{2}{\pi}} \int_0^\infty f(t) \sin kt \, dt = F_s(k) \quad (2.36)$$

Then,

$$f(t) = \sqrt{\frac{2}{\pi}} \int_0^\infty F_s(k) \sin kt \, dk \quad (2.37)$$

In our case  $k = w - w_n$  and  $f(t) = e^{-t/\tau_n}$  integral (2.36) becomes,

$$F(w - w_n) = \sqrt{\frac{2}{\pi}} \int_0^\infty e^{-t/\tau_n} \sin(w - w_n) t \, dt \quad (2.38)$$

From Fourier integral tables, for  $f(t) = e^{-at}$  by substituting in equation (2.36)  $F_s(k) =$

$\sqrt{\frac{2}{\pi}} \frac{k}{(a^2 + k^2)}$  then equation (2.36) becomes:

$$\sqrt{\frac{2}{\pi}} \int_0^\infty e^{-at} \sin kt \, dt = \sqrt{\frac{2}{\pi}} \frac{k}{(a^2 + k^2)} \quad (2.39),$$

divided both sides on  $\sqrt{\frac{2}{\pi}}$

$$\int_0^\infty e^{-at} \sin kt \, dt = \frac{k}{(a^2 + k^2)} \quad (2.40)$$

$$\int_0^\infty e^{-t/\tau_n} \sin(w - w_n) t \, dt = \frac{w - w_n}{\left(\left(\frac{1}{\tau_n}\right)^2 + (w - w_n)^2\right)} \quad (2.41)$$

Substitute equation (2.41) in (2.35):

$$C_1 = \frac{a_n}{w\tau_n} \frac{w - w_n}{\left(\left(\frac{1}{\tau_n}\right)^2 + (w - w_n)^2\right)} - \frac{a_p}{w\tau_p} \frac{w - w_p}{\left(\left(\frac{1}{\tau_p}\right)^2 + (w - w_p)^2\right)} \quad (2.42)$$

$$C_1 = \frac{a_n \tau_n (w - w_n)}{w(1 + (w - w_n)^2 \tau_n^2)} - \frac{a_p \tau_p (w - w_p)}{w(1 + (w - w_p)^2 \tau_p^2)} \quad (2.43)$$

But  $w \gg w_{n,p}$  so equation (2.43) becomes

$$C_1 = \frac{a_n \tau_n w}{w(1 + (w - w_n)^2 \tau_n^2)} - \frac{a_p \tau_p w}{w(1 + (w - w_p)^2 \tau_p^2)} \quad (2.44)$$

$$C_1 = \frac{a_n \tau_n}{1 + (w - w_n)^2 \tau_n^2} - \frac{a_p \tau_p}{1 + (w - w_p)^2 \tau_p^2} \quad (2.45)$$

Then [36],  $C(w) = C_0 + \frac{a_n \tau_n}{1 + (w - w_n)^2 \tau_n^2} - \frac{a_p \tau_p}{1 + (w - w_p)^2 \tau_p^2}$  (2.46)

## 2.5: Temperature effect on metal insulator transitions

The metal insulator transition (MIT) is defined as the vanishing of the conductivity ( $\sigma$ ) at temperature  $T$  [40]. The motion through the system's phase space often implies a change from one material to another. Since there are a variety of "metallicity parameters" indicative of the distance from the transition (like the degree of disorder, the band overlap, impurity concentration, etc) [40]. Rarely, the MIT can be passed through in a reversible manner happens only by just varying some external parameters rather than the properties of the sample [40]. The external parameters include the impurity localized electronic wave function, magnetic field and the temperature in such a way that one can pass the transition thereby changing the overlap of the impurity localized electronic wave function or by varying the magnetic field applied to the system [40]. One must extrapolate the temperature dependences to establish the occurrence of the transition. A MIT in monolayer  $\text{MoS}_2$  was found to be allowed for the high levels of doping achieved in dual gate devices [41] and this material was found to have an applications as capacitance devices [42].

Verwey reported in 1939 that bulk  $\text{Fe}_3\text{O}_4$ , which is at room temperature fairly conductive with a half-metallic character, becomes electrically insulating below 123 K (MIT point), which is now called the Verwey transition temperature ( $T_v$ ) [43]. During the last two decades, iron oxide (magnetite ( $\text{Fe}_3\text{O}_4$ ) and maghemite ( $\gamma\text{-Fe}_2\text{O}_3$ )) nanocrystals have been investigated for their various biomedical applications including magnetic biosensors, heating mediators for magnetic fluid hyperthermia and magnetic resonance imaging (MRI) contrast agents [43-45]. It is found that there is a MIT very close to room temperature for vanadium dioxide ( $\text{VO}_2$ ) that is of great practical importance as it have very fast switching between metallic and insulating phases which can be used for device applications [46-47].



## Chapter Three

### Experimental Details

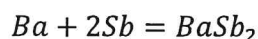
#### 3.1 Alloys formation

In this work, a quartz tube was installed in to wrapped tungsten wire evaporation source for testing its ability to bear the heating and to know the maximum temperature ( $T_{\max}$ ) that the evaporation source could reach. The evaporation source contains a K-type thermocouple for temperature measuring. The thermocouple is connected to temperature controller which reads the temperature. Our work showed that the maximum temperature is 735 °C, the quartz tube could bear 1800 °C so the 735 °C is good since it is in the range of its bearing ability. That test gave the passport to use the quartz tube wrapped with a tungsten wires for preparing alloys. The selected Ba and Sb metals have melting points of 730 °C and 630 °C , respectively. The quartz tube and related apparatus are shown in figure 3.1.



Fig 3.1: The illustration of the quartz boat in the evaporation source (item 1 for Shutter ,item 2 for quartz boat , item 3 for thermocouple ) .

Ba is a soft, silvery white metal and its atomic weight (average mass of the atom) is 137.327 g/mol. It has a body centered cubic (bcc) structure [16] and a lattice constants ( $a$ ) 5.028 Å. Sb powder which is an extremely brittle metal of a flaky, crystalline texture, it is bluish white and has a metallic luster with atomic weight of 121.76 g/mol. It has a simple trigonal structure [19] with lattice parameters of 4.307 Å, 4.307 Å and 11.273 Å and  $\gamma=120$ . These two metals were used to form a 1.27 g Ba-Sb binary alloys by mixing 0.46 g Ba which was under cyclohexene from oxidation and 0.81 g antimony powder (Sb) into a quartz tube wrapped with a tungsten wire. During heating the mixture is covered by quartz piece to avoid evaporating Sb out of the tube since it have smaller melting temperature. The melted mixture was kept under vacuum media of  $10^{-5}$  mbar at 735 C° nearly 3 minutes. The ratio of mixing 36% for Ba and 64% for Sb. This ratio is determined from their molar mass ratio according to the following relation:



$$137.33 \text{ g/mole} + 2(121.75 \text{ g/mole}) = 380.83 \text{ g/mole}$$

$$\text{For Ba : } \frac{137.33}{380.83} * 100\% = 36\%$$

$$\text{For Sb: } \frac{243.5}{380.83} * 100\% = 64\%$$



Fig 3.2: Evaporation source.

For any alloy cycle, the following procedure must be followed:

- 1- Replace the Evaporation boat with the quartz boat (quartz tube wrapped with a tungsten wires).
- 2- Connect the temperature controller with the device, putting it in the temperature measure.
- 3- Put the appropriate ratio of the metals that will form the alloy in the quartz boat.
- 4- Close the evaporation source system, the shutter, vent valve (moves clock wise) and the chamber.
- 5- Turn on the main power and wait the loading till finished.
- 6- Turn on the roughing pump and wait till the vacuum pressure reaches (10) mbar.

- 7- Turn on the turbo pump and wait until the pressure reaches ( $1 \times 10^{-5}$ ) mbar.
- 8- Start increasing the current gradually, during that, watch the reading of temperature controller till it reaches the melting temperatures of the mixing metals.
- 9- When the desired temperature is reached, wait few minutes then turn off the current.
- 10- Wait the evaporation source for cooling, then turn off the turbo pumps.
- 11- Wait until the pressure reaches 10 mbar and open the system.

The obtained BaSb<sub>2</sub> alloys were subjected to two techniques in order to investigate the structural properties of the binary alloys. Namely they are the X-ray diffraction technique (XRD) by Miniflex 600 X-ray diffractometer and scanning electron microscopy (SEM) using coXem-200 microscope.

### 3.2 X-ray diffraction (XRD)

The alloys' structure can be known using the diffraction principle of the electromagnetic wave which can be described using Bragg equation. In general, when a continuous coolimated beam of X-ray is incident on a crystal, if the path difference of the beam reflected from the upper surface and the one reflected from the lower surface is an integral multiples of the incident wavelength, a constructive interference will occur and applying Bragg's law [48].

The bulk was characterized using the Rigaku Miniflex 600 diffractometer provided with K<sub>α</sub> radiation of a copper anode of wavelength 1.5405 Å , 2θ step size 0.1° , scan rate 1°/min and θ range 10<sup>0</sup>-70<sup>0</sup> (see figure 3.3 ). The RiKago Miniflex 600 diffractometer



consists of a source of x-ray, collimator focusing the X-ray beam and a device to control the wavelength range, holder for the films , radiation detector and signal processor [49]. A “Crysdiff” software packages were used to investigate that the alloy prepared was  $\text{BaSb}_2$  by comparing it with the XRD data. The obtained XRD data were analyzed using “TREOR 92” software packages.

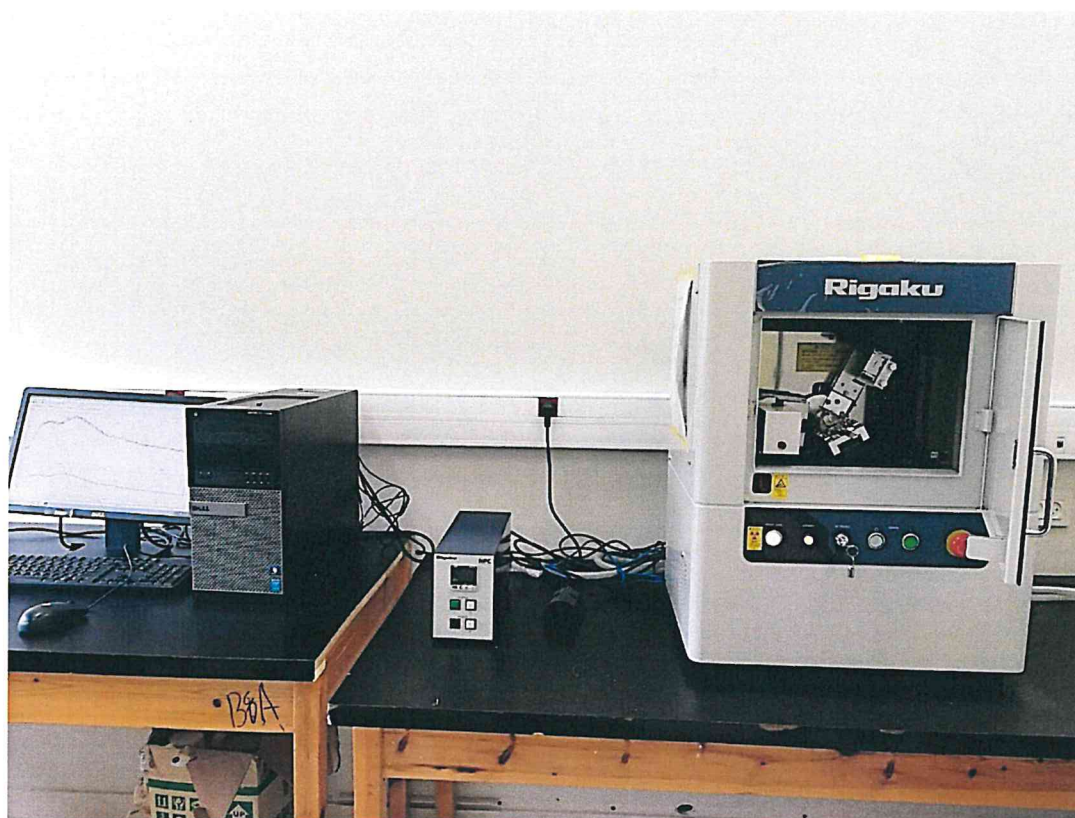


Fig 3.3: The Rigaku Miniflex 600 diffractometer.

### 3.3 Scanning electron microscopy (SEM)

CoXem-200 scanning electron microscopy (SEM) instrument was exploited to characterize the surface morphology of  $\text{BaSb}_2$  bulk alloys. Generally, a focused beam of electrons was used in this technique to scan the surface of the sample by secondary

electrons that will be produced by inelastic collisions of primary electrons, then they were ejected from the sample since they are attracted to a grid under low potential, then accelerated by a higher potential toward the detector. The primary electrons with energy range from few keV to 30 keV are created by the field emission gun. On the other hand, the secondary electrons have energies lower than that of the primary electrons by a factor of thousand. Thus, the electrons are emitted from a region that is a few angstroms from the surface of the sample. The emitted electrons signals were used to plot a x-y position. So in order to image samples, the beam is focused by a magnetic lens and then raster-scanned on a surface [50].

In our case SEM is used to image the  $\text{BaSb}_2$  bulk at several zoom factors for several layer of the bulk specimen some of them at voltage 20 KeV and the others at 28 KeV.

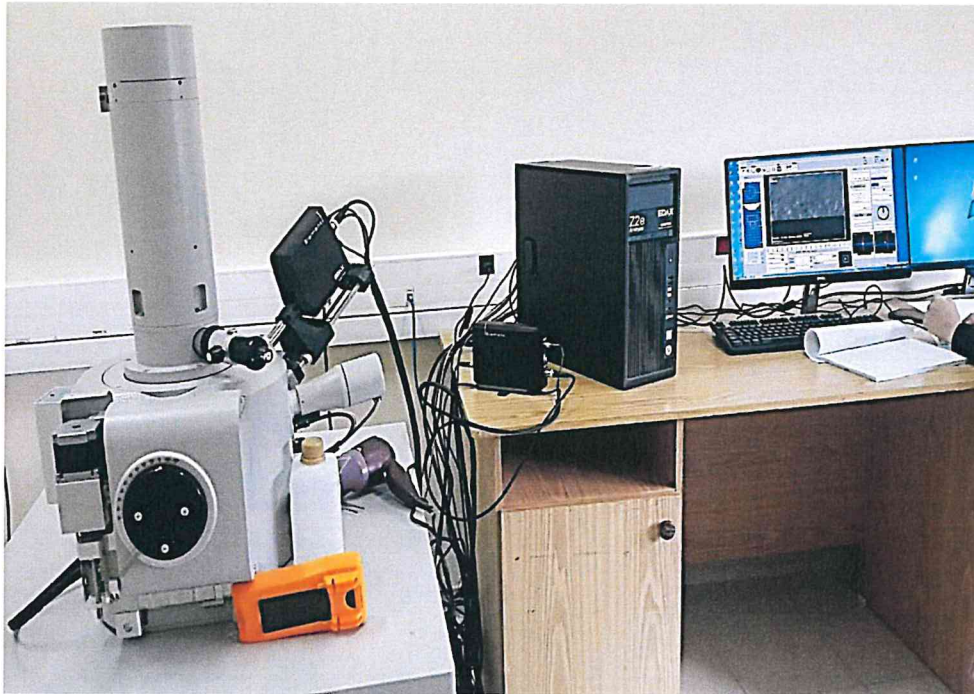


Fig 3.4: The illustration of the SEM.

### 3.4 Impedance spectroscopy measurements

The BaSb<sub>2</sub> was characterized by an impedance analyser in the frequency domain (10-1800) MHz using Agilent 4291B analyser at room temperature. The instrument was connected as RLC circuit so that the impedance ( $Z$ ), the capacitance on series ( $C_s$ ) and parallel ( $C_p$ ), the resistance ( $R$ ) and the conductance ( $G$ ) can be measured with the help of MATLAB software.

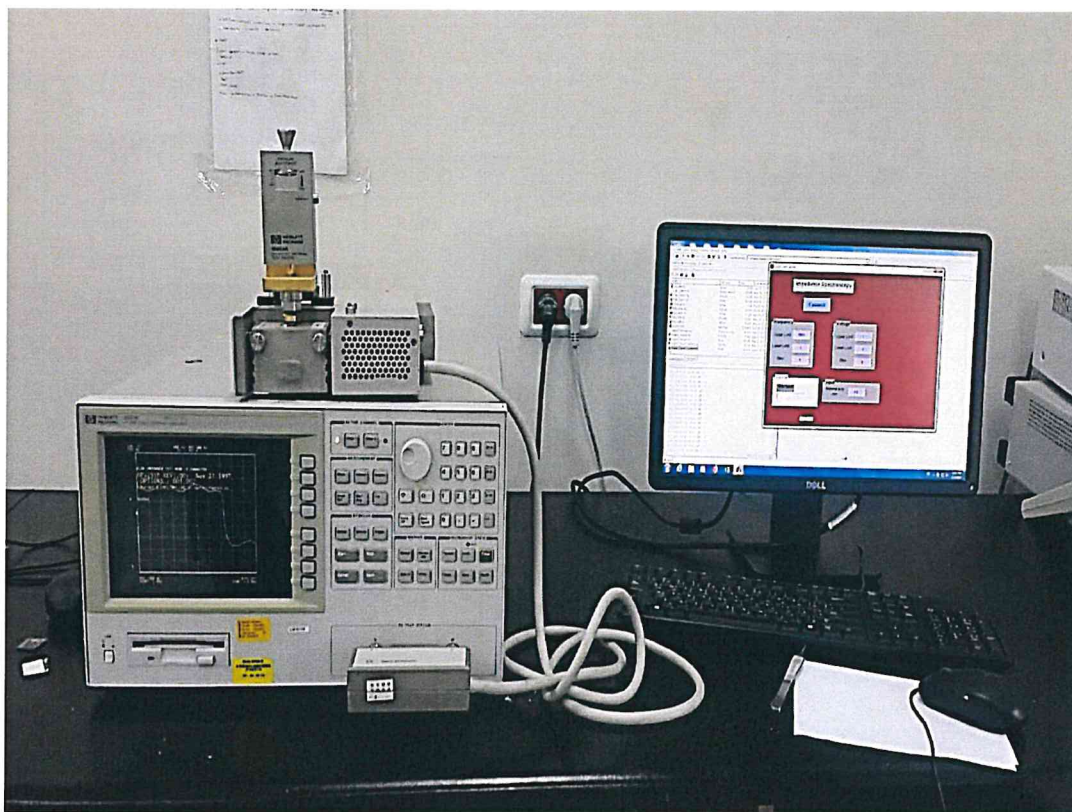


Fig 3.5: Impedance analyser.



### 3.5 Current-Voltage (IV) Measurements:

The current values with respect to the applied voltage were measured for the BaSb<sub>2</sub> bulk using Keithley 6485 picoammeter and Keithley 230 programmable voltage source with the help of a MATLAB software connected with them by a computer shown in Figures (3.6-3.7). The current-voltage (IV) measurements were recorded at room temperature (300K) for the bulk in order to know the metals' conductivity behaviour (Ohmic or not Ohmic) while the current-temperature (I-T) dependence carried out using electrical cooling (300-20) K which showed a very interesting result as we will see in the next chapter. The current-temperature data was used to form the resistivity-temperature dependence curve. The dimensions of the sample (the width (W) and the length which is the distance between the electrodes (L)) were measured by a ruler and found to be 0.3 cm and 0.4 cm, respectively as see in figure 3.6 while the thickness (t) was measured by micrometer and found to be 0.056 cm. According to that measurement it is clearly found that the area (A) is 0.0168 cm<sup>2</sup> which helped in resistivity calculations.

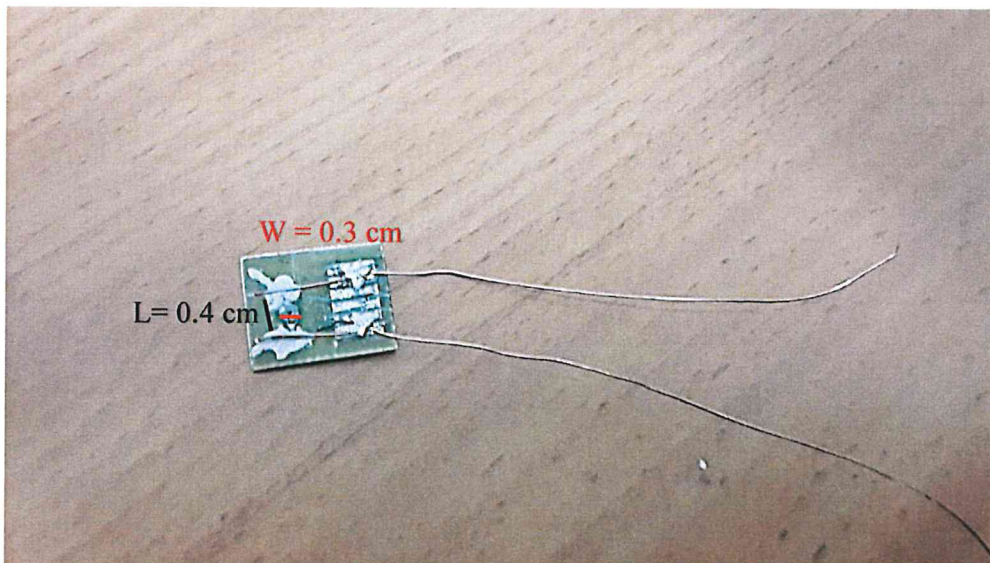


Fig 3.6: the prepared BaSb<sub>2</sub> bulk sample for the IV measurement.



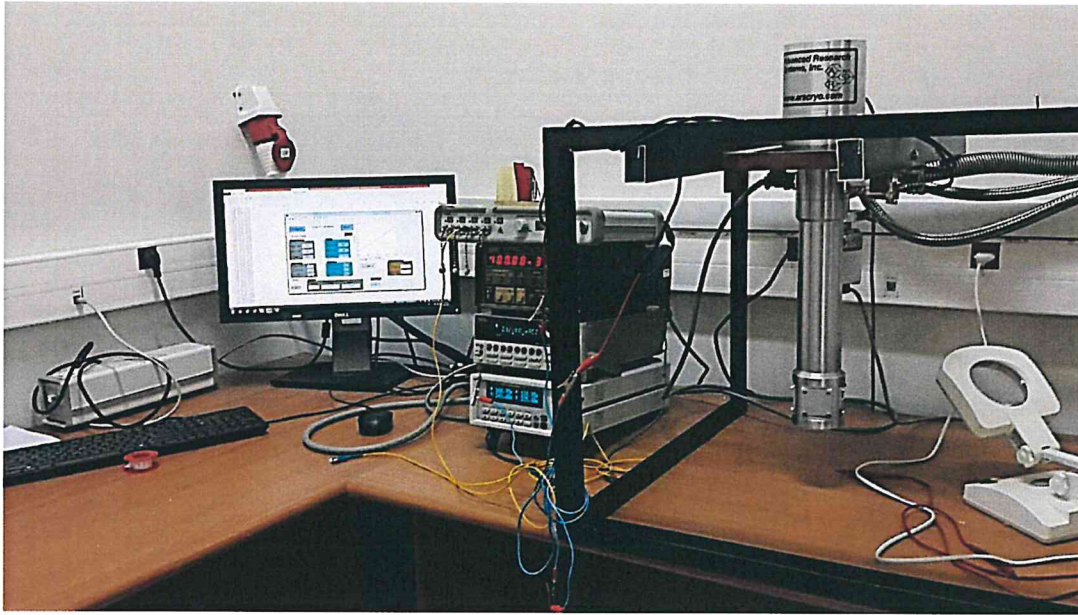


Fig 3.7: IV measurements.

## Chapter Four

### Results and Discussion

#### 4.1 XRD results:

BaSb<sub>2</sub> alloys are prepared from the high purity Ba (99.99%) and Sb (99.99%) in stoichiometric compositions. The alloys were achieved through raising the temperature to 735 C° and keeping the melted alloy for few minutes under vacuum pressure of 10<sup>-5</sup> mbar. The resulting X-ray diffraction patterns for the alloys are shown in figure 4.1. As seen from the figure crystalline phase of BaSb<sub>2</sub> is obtained. The X- ray patterns comprise 16 sharp peaks. The peak with the maximum height is centred at  $2\theta = 59.1^\circ$  with an intensity of  $1.69 \times 10^3$  a.u. To identify the crystal structures of the obtained alloys the “Crysdiff” and “TREOR 92” software packages were employed.

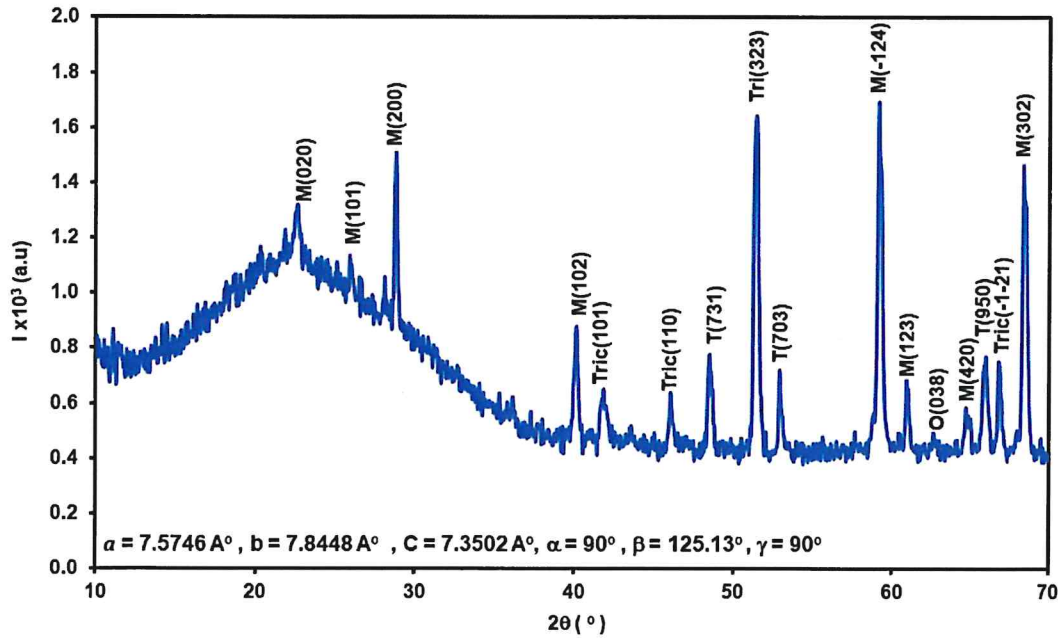


Fig 4.1: The XRD patterns for BaSb<sub>2</sub> alloys.

The expected reflections peaks of the possible formed materials are estimated by “Crysdiff” software packages assuming well known lattice parameters. Particularly, the “Crysdiff” software packages were used to know which alloy was prepared ( $\text{BaSb}_2$ ,  $\text{BaSb}_3$ ), if any oxides were formed such as ( $\text{BaO}$ ,  $\text{Sb}_2\text{O}_3$ ) and if any of the Ba and Sb are still not fused. Inserting the theoretical lattice parameters, phase group and theoretical structure of the expected alloys, the “Crysdiff” software as a response to that entered data showed the values of theoretically expected diffraction angles ( $2\theta$ ). The results are shown in table 4.1. The percentage differences between the  $2\theta$  of the expected materials and the observed  $2\theta$  values known as diff % are also shown in the table. As the table shows not all the peaks of the expected alloys appeared in the assumed structures. The diff % between the observed and the expected diffraction angle for Ba, Sb,  $\text{BaSb}_2$ ,  $\text{BaSb}_3$ ,  $\text{Sb}_2\text{O}_3$  and BaO is very large indicating that the currently obtained alloys exhibit different structure from these already known types. The diff % between the expected formed material and the experimentally observed is shown in table 4.2. None of the experimentally observed peaks can be assigned to Ba, Sb,  $\text{Sb}_2\text{O}_3$  and BaO. For this reason, we went to the believing that the obtained alloys refer to some yet unknown phases of  $\text{BaSb}_2$  or  $\text{BaSb}_3$ . A deep comparison led to the exclusion of the metals and oxide due to their high diff % values and the absence of some or many diffraction angles  $2\theta$  makes the expectations narrower. The comparison was reduced to the expected Ba-Sb binary alloys ( $\text{BaSb}_2$ ,  $\text{BaSb}_3$ ). It seemed that most of the expected peaks appeared in the calculated  $\text{BaSb}_2$  alloys and all of them in the calculated  $\text{BaSb}_3$  alloys with a diff % value between the experimental or the observed peaks and the calculated ones. For the calculated  $\text{BaSb}_2$  alloys the diff % range (2.8- 44.24) % with 5.74% for the maximum observed peak at  $59.1^\circ$ . For the  $\text{BaSb}_3$  calculated alloys, the diff % range is (0.14- 98.44) % with 44.95%

at the same angle of diffraction. So since the diff % range of the  $\text{BaSb}_2$  calculated alloys were smaller than of the range of the calculated  $\text{BaSb}_3$  alloys and because the maximum observed peak diff % for the calculated  $\text{BaSb}_2$  alloys were smaller than of that for the  $\text{BaSb}_3$  calculated alloys, we concluded that the prepared Ba-Sb binary alloys were mostly  $\text{BaSb}_2$  alloys.

Careful analysis using “TREOR 92” software packages to solve the structure and determine the lattice parameters were carried out. The analysis included all possible types of structures and considered the difference percentages between the observed and calculated  $2\theta$  (diff%) values. This issue is actualised through inserting the observed peaks with the intensity and the expected structure into the software. Table 4.3 shows the diff % values of the different structure of the  $\text{BaSb}_2$  alloys. “TREOR 92” software packages were directed to obtain the lattice parameters and plane orientations of the peaks assuming all possible seven types of structures. However, the cubic structure was excluded since it was not containing all the exponentially observed peaks. The absence of the peaks indicates that the experimentally obtained structure is more complicated and may be assigned to more complicated structural phases. The diff % ranges for the other structures were (0-13.7) % for monoclinic, (0-9.8) % for orthorhombic, (0-38) % for hexagonal, (0-38) % for trigonal, (0-9.5) % for tetragonal and (0-55.8) % for the triclinic. By comparing the ranges, cubic, hexagonal and trigonal structures were excluded, respectively. The triclinic, monoclinic structural phases and the orthorhombic were found to contain more zeros diff % values than tetragonal structure. Since the diff % values at this maximum are very close together, the number of zeros in each structure is the decisive. So when assuming one structural phase, tetragonal was also excluded. After that result, we started to compare the diff % between the monoclinic, triclinic , tetragonal, trigonal and

orthorhombic structures. Based on smaller value, the peak is assigned to the associated structure. By that way it was found that some of peaks related to the tetragonal, orthorhombic, trigonal and the others to triclinic and monoclinic. The tabulated data and its related analysis led to the thought that more than one structural phase do exist in this material. Thus, the material is composed of monoclinic BaSb<sub>2</sub> as the dominant structure (absolute peak with maximum height and least error) as it was related to the peak with the maximum height at  $2\theta = 59.1^\circ$  and tetragonal as secondary dominant phase and orthorhombic, trigonal and triclinic as very minor phases.

Table 4.1: The “Crysdiff” software data that include the theoretical values of  $2\theta$  the associated diff % for Ba, Sb, BaSb<sub>2</sub>, BaSb<sub>3</sub>, Sb<sub>2</sub>O<sub>3</sub> and BaO.

$2\theta$ Exp	$2\theta$	diff %	$2\theta$	diff %	$2\theta$	diff %	$2\theta$	diff %	$2\theta$	diff %	$2\theta$	diff %	$2\theta$	diff %	$2\theta$	diff %
BaSb <sub>2</sub>	Ba		Sb		BaSb <sub>2</sub>		BaSb <sub>3</sub>		Sb <sub>2</sub> O <sub>3</sub>		Sb <sub>2</sub> O <sub>3</sub>		BaO		BaO	
bulk					monoclinic				orthorhombic		cubic		tetragonal		cubic	
22.65			23.66	100.68	22.54	10.75	22.62	3.23								
25.90			25.13	77.40			25.67	23.27	25.49	40.82						
28.80	30.82	202.42	28.67	12.61	28.97	16.56	28.80	0.38	28.63	16.78			28.69	11.28		
40.15			40.06	8.54	40.59	44.24	40.69	53.92					40.44	28.99		
41.85			41.91	6.48	41.41	43.85	41.85	0.14					41.02	83.22		
46.05			47.06	100.59	46.02	2.80	46.06	1.36			46.55	49.53				
48.50			48.40	9.51	48.92	41.79	48.23	27.00	47.03	147.18						
51.40	51.44	4.12	51.57	17.40	51.33	7.40	51.56	16.49			51.17	23.02	50.33	106.81		
52.90					52.47	43.17	52.75	15.03								
59.10			59.37	27.23	59.04	5.74	58.65	44.95	59.28	17.92			59.40	30.19		
60.90	61.18	27.99			60.76	14.45	60.96	6.18								
62.60			62.79	19.39			62.61	1.13	63.30	69.78						
64.65	64.22	43.37	64.82	17.25	64.90	24.67	64.39	26.11								
65.90			65.92	2.06	65.98	7.61	65.71	19.29					65.63	26.75		
66.70			66.82	11.79	66.88	18.27	67.68	98.44	66.82	11.61	66.56	13.54	66.87	16.83	66.56	13.54
68.25			68.55	30.28	68.01	23.64	68.29	3.95	68.53	28.00			67.28	97.23		

Diff %: The percentage difference between the calculated  $2\theta$  and the experimental ones.

Table 4.2: The “Crysdiff” software data include only the diff% values to obvious view for the differences between the experimental  $2\theta$  and the calculated or theoretical ones.

<b>2<math>\theta</math> Exp</b>	<b>diff %</b>	<b>diff %</b>	<b>diff %</b>	<b>diff %</b>	<b>diff %</b>	<b>diff %</b>	<b>diff %</b>	<b>diff %</b>
<b>BaSb<sub>2</sub></b>	<b>Ba</b>	<b>Sb</b>	<b>BaSb<sub>2</sub></b>	<b>BaSb<sub>3</sub></b>	<b>Sb<sub>2</sub>O<sub>3</sub></b>	<b>Sb<sub>2</sub>O<sub>3</sub></b>	<b>BaO</b>	<b>BaO</b>
<b>bulk</b>					<b>orthorhombic</b>	<b>cubic</b>	<b>tetragonal</b>	<b>cubic</b>
22.65		100.68	10.75	3.23				
25.9		77.4		23.27	40.82			
28.8	202.42	12.61	16.56	0.38	16.78		11.28	
40.15		8.54	44.24	53.92			28.99	
41.85		6.48	43.85	0.14			83.22	
46.05		100.59	2.8	1.36		49.53		
48.5		9.51	41.79	27	147.18			
51.4	4.12	17.4	7.4	16.49		23.02	106.81	
52.9			43.17	15.03				
59.1		27.23	5.74	44.95	17.92		30.19	
60.9	27.99		14.45	6.18				
62.6		19.39		1.13	69.78			
64.65	43.37	17.25	24.67	26.11				
65.9		2.06	7.61	19.29			26.75	
66.7		11.79	18.27	98.44	11.61	13.54	16.83	13.54
68.25		30.28	23.64	3.95	28		97.23	

Table 4.3: Data was given by "TREOR 92" software shows the entered experimental  $2\theta$ , their associated intensity and what the diff % for each expected structure.

$2\theta$ Exp	I	diff %	diff %	diff %	diff %	diff %	diff %	diff %
BaSb <sub>2</sub>		monoclinic	orthorhombic	cubic	hexagonal	trigonal	tetragonal	triclinic
bulk								
22.65	1318	0	0		0	0	0	0
25.9	1131	0	0		0	0	0	0
28.8	1506	0	0	0	5.7	5.7	4.5	0
40.15	877	0	3.3		38	38	6.5	0
41.85	651	1.6	1.6	66.7	0	0	5	0
46.05	638	8.3	6.6		9.5	9.5	0.5	0
48.5	776	13.7	4	37	2.8	2.8	0.2	41.1
51.4	1642	8.3	4.9		1.1	1.1	2.1	1.5
52.9	716	4.6	9.8		5	5	0.4	12.3
59.1	1690	2.1	4.7	55.4	4.5	4.5	2.9	16
60.9	683	0.1	5.4		5.4	5.4	8.5	11.5
62.6	494	9.1	0.4		0.5	0.5	9.5	55.8
64.65	585	0.3	2.2		0.7	0.7	0.9	2.2
65.9	770	8.1	1.2		5.7	5.7	1.1	22.4
66.7	750	2.5	1.9		1.7	1.7	2.5	1.5
68.25	1456	1.9	7.3	67.9	7.8	7.8	6.9	15.3



As we concluded from the analysed “Crysdiff” software data and the “TREOR 92” software data, the prepared alloys were BaSb<sub>2</sub> and exhibiting both of the monoclinic and other minor phases. Our calculations of "phywe measure 4 " data (see table 4.4) showed that the weight percentages of the monoclinic structure is 58.46% while that of others are 41.54%.

Table 4.4: Data obtained from " phywe measure 4 " software.

<b>2<math>\theta</math> (°)</b>	<b>Structure</b>	<b>Area(cm<sup>2</sup>)</b>
<b>22.65</b>	Monoclinic	1144.90
<b>25.90</b>	Monoclinic	572.70
<b>28.80</b>	Monoclinic	927.77
<b>40.15</b>	Monoclinic	549.95
<b>41.85</b>	Triclinic	515.75
<b>46.05</b>	Triclinic	403.57
<b>48.50</b>	Tetragonal	670.22
<b>51.40</b>	Trigonal	940.72
<b>52.90</b>	Tetragonal	491.48
<b>59.10</b>	Monoclinic	1141.80
<b>60.90</b>	Monoclinic	343.27
<b>62.60</b>	Orthorhombic	379.42
<b>64.65</b>	Monoclinic	418.67
<b>65.90</b>	Tetragonal	540.30
<b>66.70</b>	Triclinic	453.77
<b>68.25</b>	Monoclinic	1085.98

According to that concluded information we returned to “TREOR 92” original obtained data to give the associated miller indices ( $hkl$ ) for each peak (see figure 4.1). Inserting the associated lattice parameters for the main structure (monoclinic)  $a$ ,  $b$ ,  $c$ ,  $\alpha$ ,  $\beta$  and  $\gamma$  by “TREOR 92” which are shown in table 4.5.

Table 4.5: The calculated lattice parameters of the prepared BaSb<sub>2</sub> alloys and the theoretical parameters of the mixing metals Ba and Sb.

	BaSb <sub>2</sub> experimental	BaSb <sub>2</sub> theoretical	BaSb <sub>3</sub>	Ba	Sb
<i>a</i> (Å°)	7.5746	5.18	10.81	5.02	4.31
<i>b</i> (Å°)	7.8448	4.36	8.52	5.02	4.31
<i>c</i> (Å°)	7.3502	9.43	6.47	5.02	11.27
$\alpha$	90.00	90.00	90.00	90.00	90.00
$\beta$	125.13	101.56	112.66	90.00	90.00
$\gamma$	90.00	90.00	90.00	90.00	120.00

Table 4.5 shows the lattice parameters of the prepared BaSb<sub>2</sub> alloys and its original mixing metals Ba and Sb. It seemed clearly that lattice dimensions *a*, *b* and *c* was increased to 7.5746 Å°, 7.8448 Å° and 7.3502 Å°, respectively, compared with Ba. The same happened when comparing with Sb except that *c* decreased from 11.27 Å° to 7.3502 Å°. From the value of  $\alpha$ ,  $\beta$  and  $\gamma$ , we could conclude that there is a change in the structure of the alloys compared with cubic Ba and trigonal Sb. This proved in the “TREOR 92” data analysis. By comparing the prepared or experimental BaSb<sub>2</sub> with the theoretical one in which the alloys are monoclinic [51], it is noticed that there is an increase in the value of *a* and *b* from 5.18 Å° and 4.36 Å° to 7.5746 Å° and 7.8448 Å°, respectively, while *c* decreased from 9.43 Å° to 7.3502 Å°. This may be assigned to the difference of structure for the prepared alloys compared with the theoretical one since that our prepared alloys is a multistructure of monoclinic and other minor phases while the theoretical one is just monoclinic. We can support our suggested explanation by looking to the changes in the values  $\beta$  from 101.56° to 125.13° which is another sign for the structure change or transition. Looking to the experimental BaSb<sub>2</sub> alloys and the BaSb<sub>3</sub> alloys there is also a

difference in the lattice parameters values which indicate a different structure and from “Crysdiff” software a different alloys.

To reveal information about the structural parameters, we have calculated the interplanar distance ( $d$ ), crystallite size ( $D$ ), stacking faults percent (SF%), dislocation density( $\delta$ ) along the  $a$ ,  $b$ ,  $c$ - axis and strain ( $\varepsilon$ ) from the broadening width ( $\beta$ ) of the maximum observed peaks using the relations (2.8-2.11). The obtained results are shown in table 4.6.

The targeted grain size usually depends on the nature of the material’s application. Generally, a good mechanical strengths suggested to be achieved if the thinnest object dimension is at least 10 times larger than the grain size [52]. That means, a 1.0 mm thick wire would exhibit a grain size in the range of 100  $\mu\text{m}$ , and a 0.1 mm thick wire would be its grain size less than 10  $\mu\text{m}$  [52]. For our obtained grain size which is 27.26 nm (0.02726  $\mu\text{m}$ ) it means that if we take a  $2.726 \times 10^{-4}$  mm thick wire of the  $\text{BaSb}_2$  alloys it would be enough to give a good mechanical strength. Decreasing the grain size in fact is the only mechanism by which both the strength and the toughness of an alloys is increased. Other mechanisms of increasing strength lead to decreases in toughness. Grain size also was found to have a noticeable effect on the risk of hot cracking [53], a small grain size was more resistant of hot cracking than a large grain size [53]. As a result comparison with titanium, zirconium and scandium [53].  $\text{BaSb}_2$  alloys bulk may be used to promote a fine grain size. These alloys forming finely dispersed solid particles in the weld metal. These particles of the alloys act as nuclei on which the grains form as solidification proceeds. As appears in table 4.6, stacking fault which is a type of defect characterizes or describes the disordering of crystallographic planes was found to be 0.21%. That value is small enough to say that the  $\text{BaSb}_2$  alloys planes structure is ordered and have very small defect which make it nearly ideal crystal. As also appears in

the table the number of dislocations in a unit volume of the crystalline BaSb<sub>2</sub> alloys along the *a*-axis, *b*-axis and *c*-axis ( $\delta_a$ ,  $\delta_b$ ,  $\delta_c$ ) are  $(1.96, 1.89, 2.02) \times 10^{11}$  lines/cm<sup>2</sup>, respectively. The positive obtained value of the strain ( $\epsilon$ )  $2.69 \times 10^{-3}$  indicated that we have a tensile strain [ 54 ].

Table 4.6: The structural parameters of monoclinic phase of BaSb<sub>2</sub> alloys.

<b>2<math>\theta</math></b>	59.1
<b>I (a.u)</b>	1690
<b>d(A<sup>0</sup>)</b>	1.56
<b>(hkl)</b>	-1 2 4
<b>D(nm)</b>	27.26
<b>SF%</b>	0.21
<b><math>\delta_a(\times 10^{11} \text{ lines/cm}^2)</math></b>	1.96
<b><math>\delta_b(\times 10^{11} \text{ lines/cm}^2)</math></b>	1.89
<b><math>\delta_c(\times 10^{11} \text{ lines/cm}^2)</math></b>	2.02
<b><math>\epsilon(10^{-3})</math></b>	2.69

#### 4.2 Scanning electron microscopy results.

The scanning electron microscopy has shown that the produced  $\text{BaSb}_2$  alloys are of layered structure as seen from figure 4.2. Figure 4.3 (a) shows an enlargement of 500 times for the three layers. A close view of the layers is shown in figure 4.3 (b), (c) and (d). Even for an enlargement of 10 K times as in figure 4.3 (d) one may observe an irregular distributions of grains. The grain accumulations are not systematic.

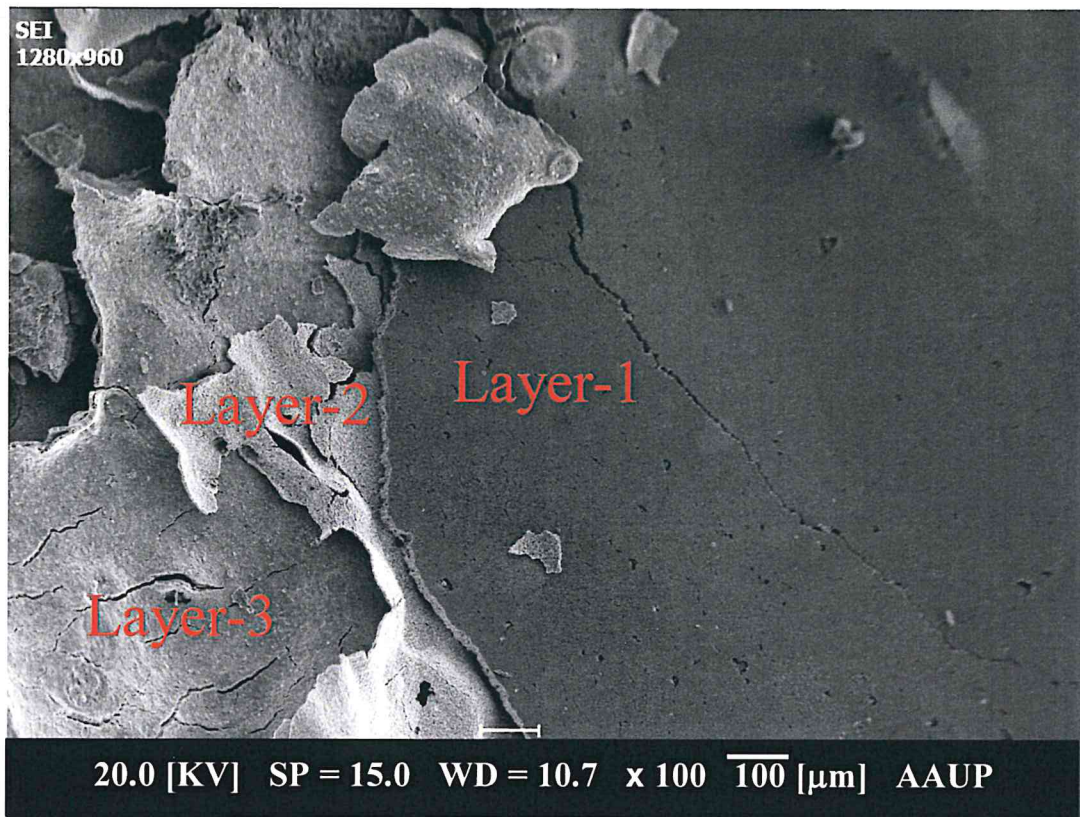
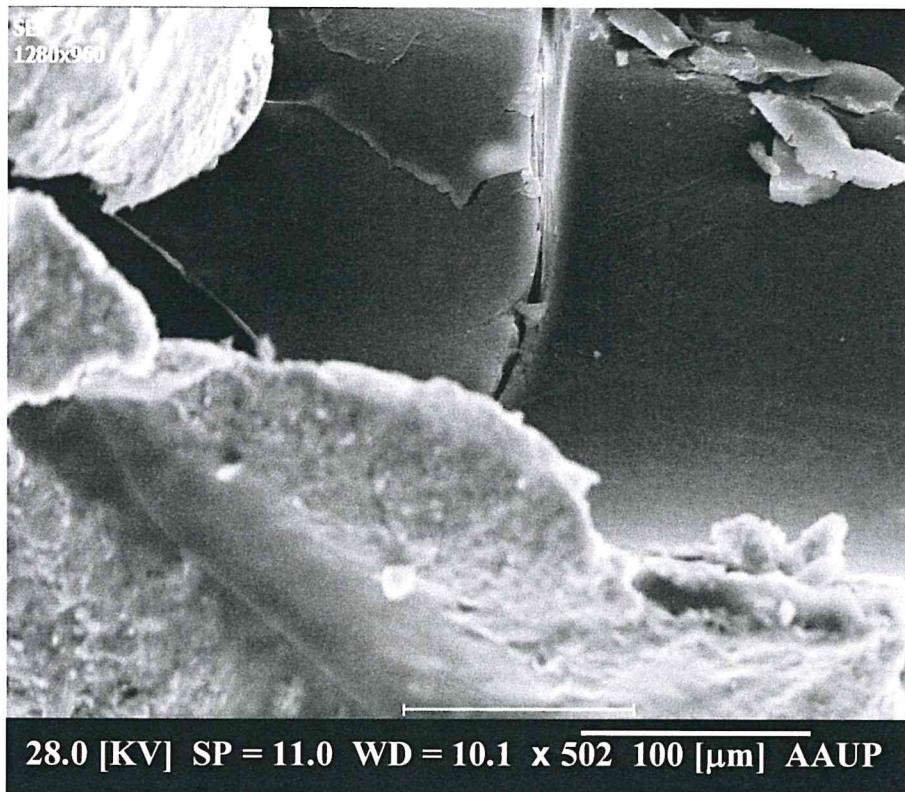


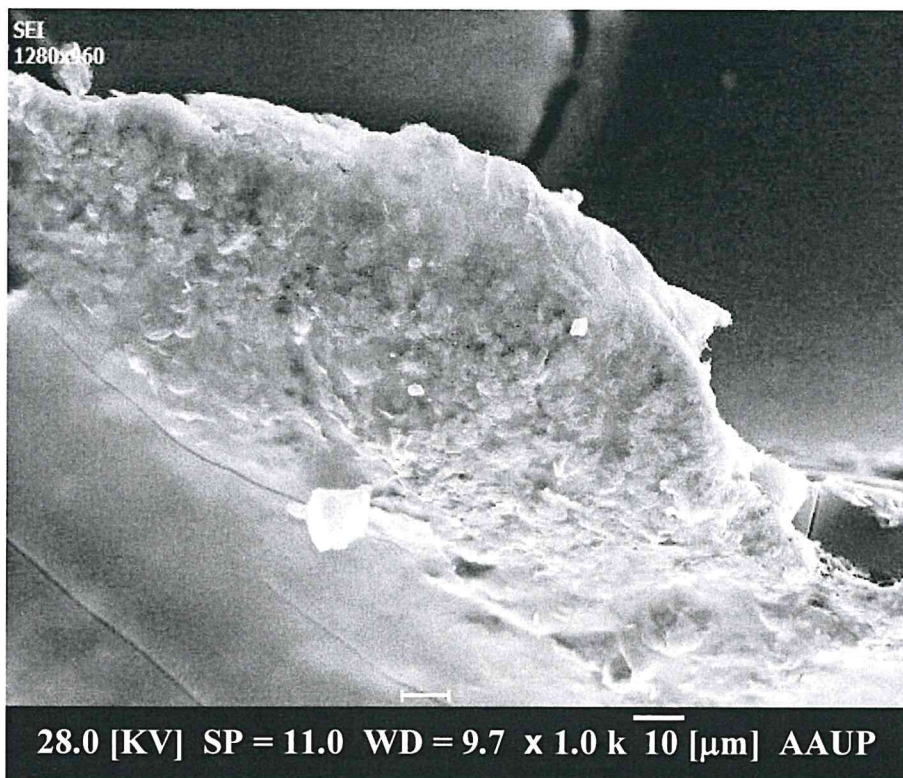
Fig 4.2: The three layers of the  $\text{BaSb}_2$  bulk at 100 amplification.



a



b



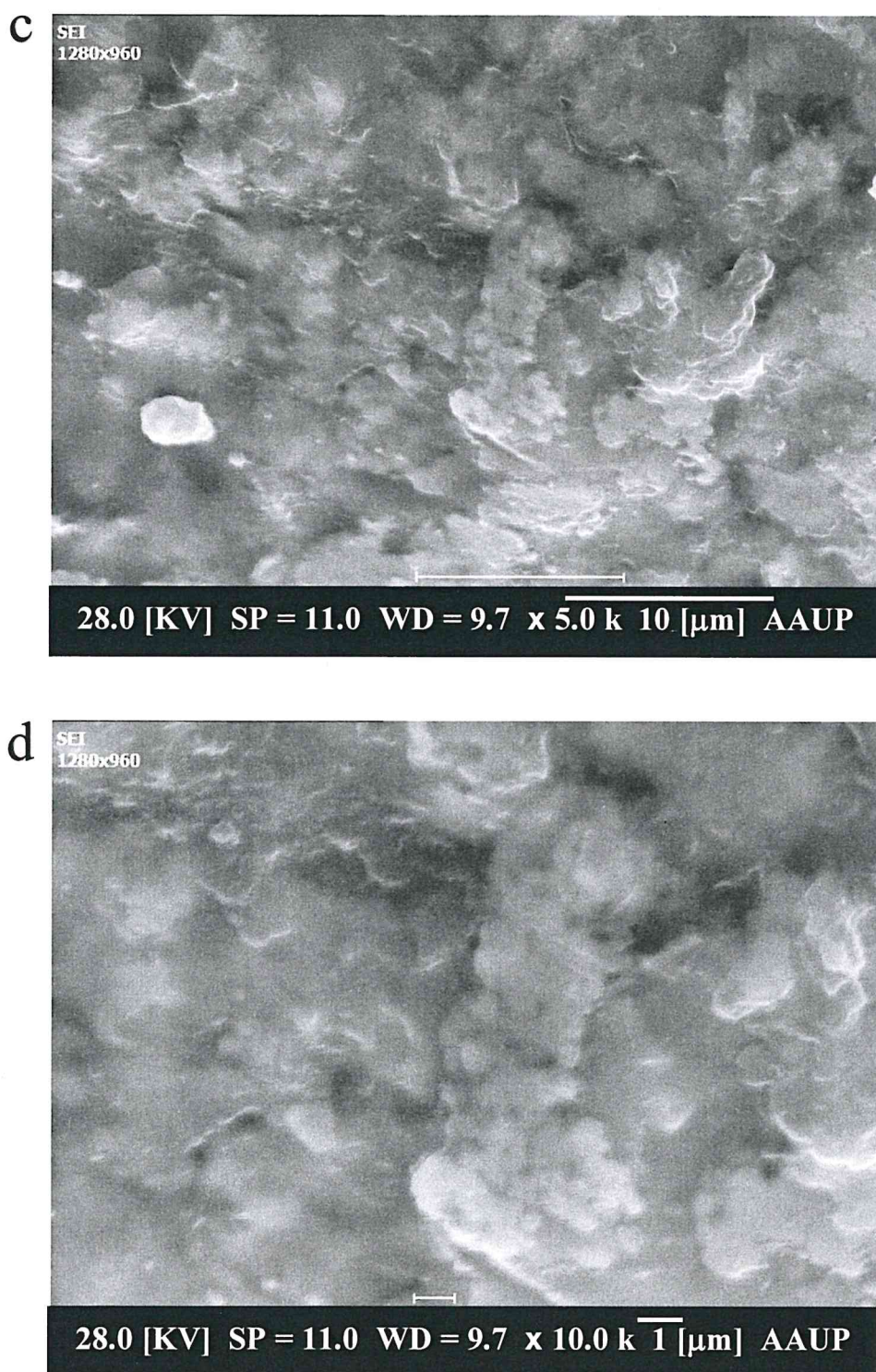
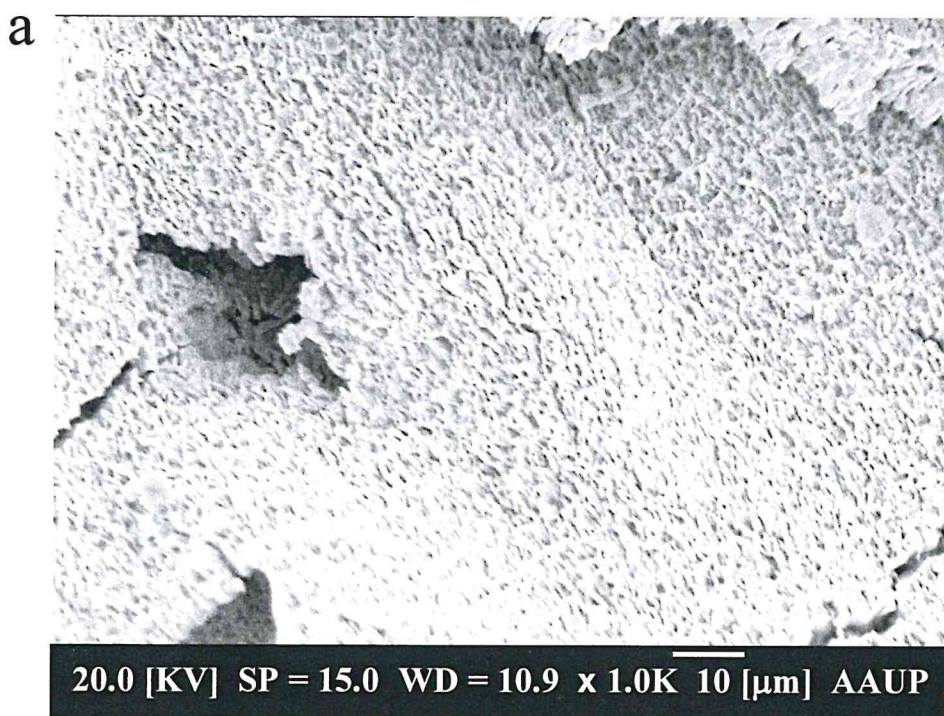


Fig 4.3: The top layer of the BaSb<sub>2</sub> bulk at different amplifications of 500, 1000, 5000, 10000 for a, b, c and d respectively.



The scanning electron microscopy images for an enlagement of 1000 times ( figure 4.4 a) which were collected from the surface of the second layer of BaSb<sub>2</sub> alloy has shown that the surface contains discontinuous cracks. Selecting an area and enlarging it 5000 times ( figure 4.4 b ) indicated that the cracks are of three different lengths and widths. These cracks appeared better when the image is enlarged 10000 times ( figure 4.4 c ). The widest crack is 1.6  $\mu\text{m}$  width and 4.5  $\mu\text{m}$  length. The narrowest are 400 nm width and 5.0  $\mu\text{m}$  length (figure 4.2 , figure 4.4a).





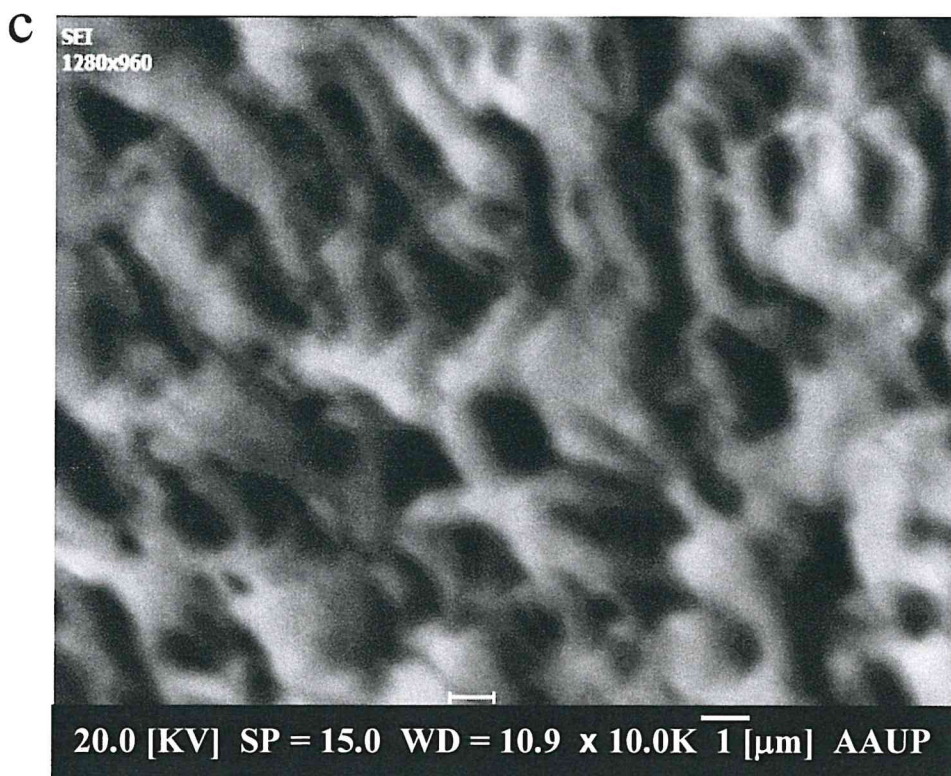
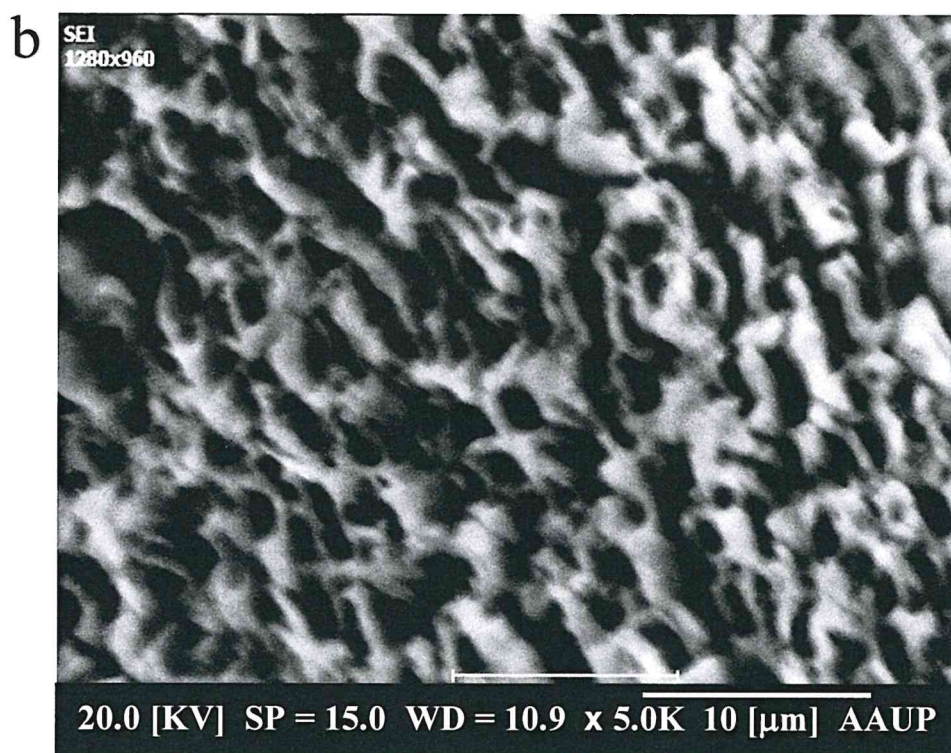
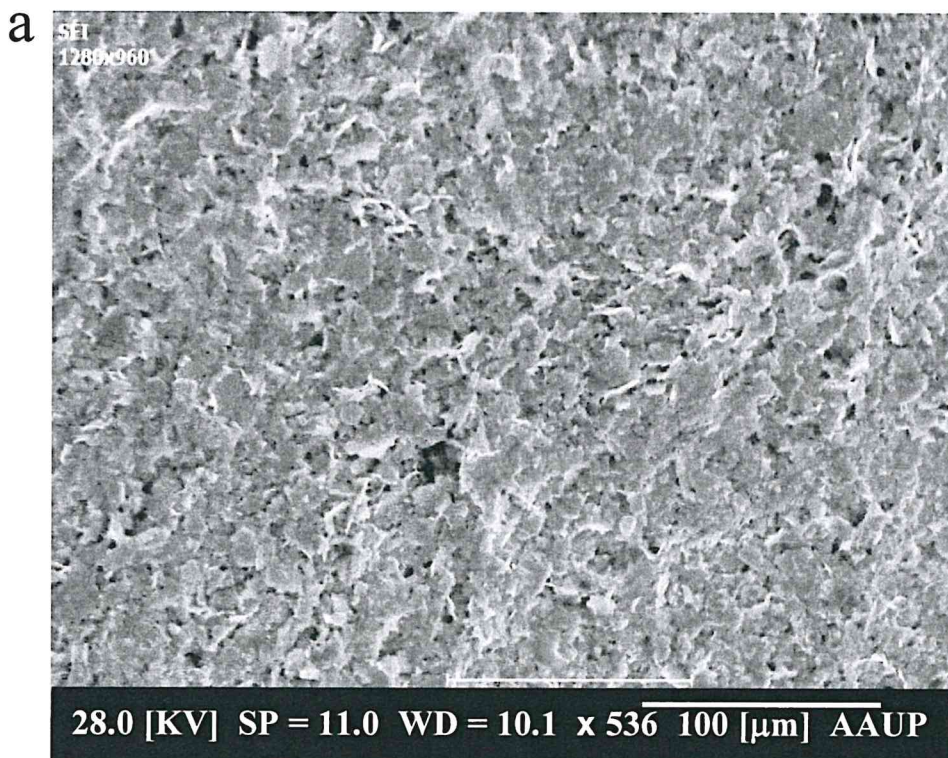


Fig 4.4: The second layer of the BaSb<sub>2</sub> bulk at different amplifications (1000, 5000, 10000) for a, b and c respectively.

Figure 4.5 display the scanning electron microscopy images for the third layer being enlarged 500, 5000 and 10000 times. The layer appears to be composed of thin peel sheets. The peels are randomly oriented and randomly distributed. The peels length could be as long as 10  $\mu\text{m}$  and exhibit width in the range of (1.6 - 5.0)  $\mu\text{m}$ .





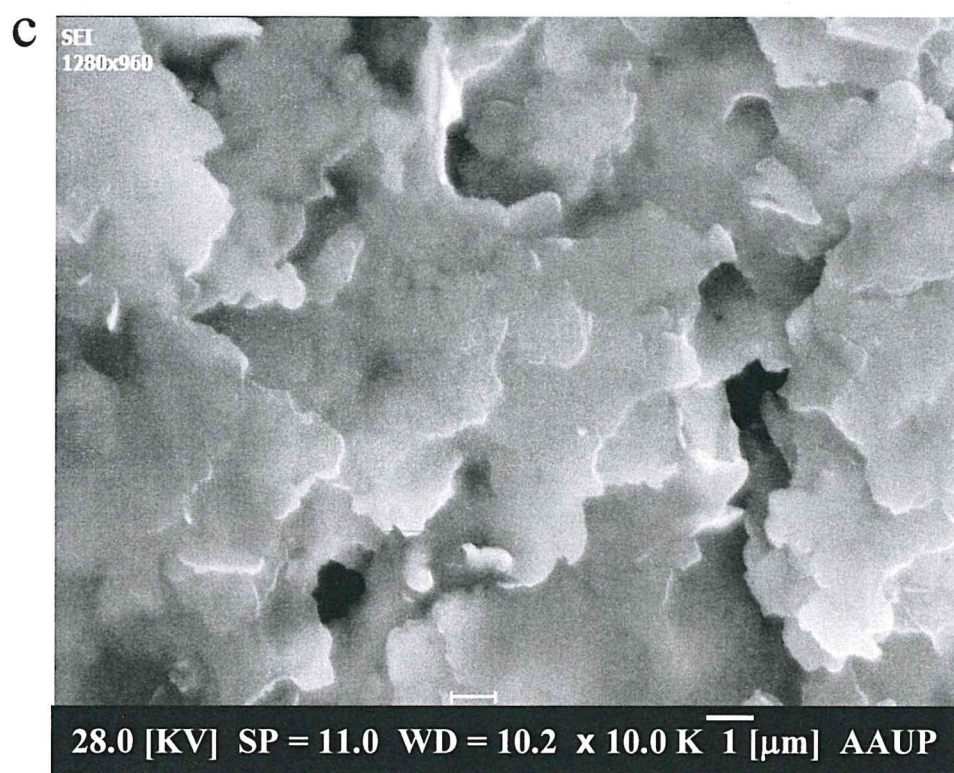
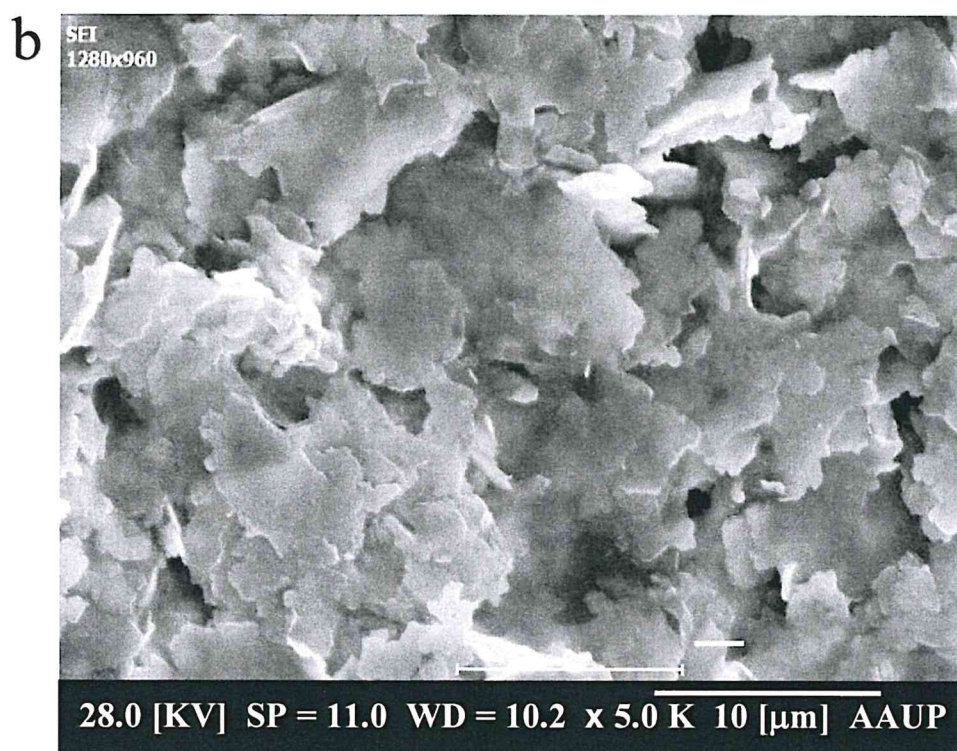


Fig 4.5: The third layer of the BaSb<sub>2</sub> bulk at different amplifications nearly (500, 5000, and 10000) for a, b and c respectively.

### 4.3 Impedance Spectroscopy

To understand the AC electrical properties of the BaSb<sub>2</sub> alloys, the bulk samples were excited with an AC signal of frequency that ranges from 0.01 to 1.8 GHz. As appeared in figure 4.6, the applied AC signal resulted in a negative capacitance values (NC). Indicating a wide range of applications. NC effect is used for vibration suppression [53] or for semi-active vibration control in synchronized switch damping techniques [55]. It is also found to be suitable for analog circuit applications in ferroelectric MOSFETS [56]. NC is useful for noise reduction [57-58]. Negative capacitance could also find uses in many other applications like batteries [59-60] and super capacitors [61-62]. When a change in charge is associated with an oppositely charging, the resultant voltage across a material electrodes behave in such a way that a decrease in voltage leads to an increase in charge, then a negative capacitance occurs [63]. This inverse relation between the charge and voltage could enhance the voltage across the common dielectric material and that gained voltage could reduce the supply voltage in a transistor so that making computers and electronic devices energetically efficient [64]. The change of the dipole energy at the interface between the different layers (as seen in SEM) of the BaSb<sub>2</sub> alloys [65] and the polarization [66] could also be accounted for the NC effect.

In order to reveal more realistic information about the physics beyond the negative capacitance effect we employed the Ershov-Qasrawi modified model for AC conduction. The model assumes that the capacitance spectra are dominated by two parts. Namely, the geometrical capacitance ( $C_0$ ) and dynamic capacitance ( $C_1$ ). The dynamic capacitance results from the dependence of the capacitance on the decaying current and on the material plasmon frequency. It assumes negative capacitance for holes and positive

capacitance for electrons. The model follows equation 2.46. In accordance with this equation C- spectra display positive values whenever electrons dominates and negative when holes are dominates provided that signals are oscillating against material plasmon frequency.

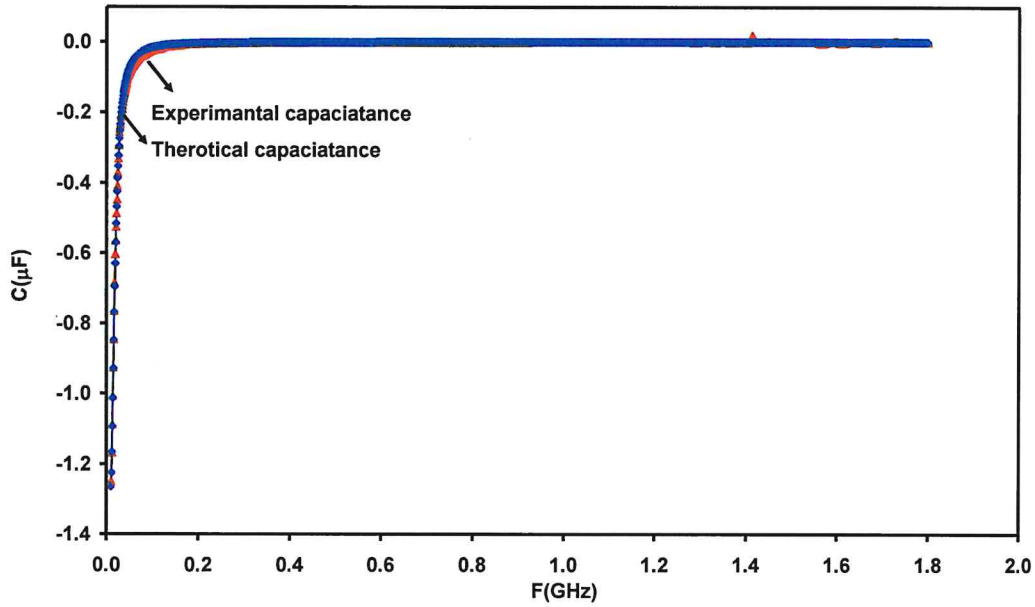


Fig 4.6: Modelling of the experimental capacitance (the red line) with the theoretical or calculated one (the blue line).

The experimental capacitance was modelled with equation 2.46 and showed a good matching as appearing in figure 4.6. This matching was accepted since most of the obtained capacitance data stick with the calculated capacitance. It means that the BaSb<sub>2</sub> alloys capacitance will behave nearly as an ideal NC devices. The good correlation between theory and experiment is achieved via the tabulated parameters shown in table 4.7. As appears in table 4.7 for a geometrical capacitance value of 10 pF as assuming a rate of change of capacitance with time ( $a_1$ ) being zero, one find  $a_2$  of 80 F/s and plasmon

frequency of 60 MHz. It means large number of holes are injected forcing decrement of the number of free electrons and resulting in the NC effect.

Table 4.7: The fitting parameters of the capacitance and conductance of BaSb<sub>2</sub> alloys.

Parameter	Value
$\tau_0$ (ps)	0.17
$\tau_{hop}$ (ns)	16.00
$\nu$ (cm <sup>-1</sup> )	200.80
$N(E_F)$ ( $\times 10^{18}$ cm <sup>-3</sup> eV)	330.00
$\sigma_L(w)$ ( $\times 10^{-3}$ $\Omega^{-1}$ cm <sup>-1</sup> )	98.00
$\sigma_H(w)$ ( $\times 10^{-5}$ $\Omega^{-1}$ cm <sup>-1</sup> )	98.00
$C_o$ (pF)	10.00
$a_n$	0.00
$a_p$	80.00
$W_n$ (GHz)	0.00
$W_p$ (GHz)	0.06

The conductance spectra of BaSb<sub>2</sub> alloys which are presented in figure 4.7 were measured in the frequency range (0.01-1.80) GHz. The conductance (G) have a maximum value nearly of 16.5  $\Omega^{-1}$  at 0.01 GHz. G started to decrease gradually till it reaches 1.0  $\Omega^{-1}$  at 0.5 GHz. This value continues to be nearly the same in the range (0.5-1.3) GHz. After this range of frequency it returns to continue decreasing but in a smaller rate till it reaches 0.01  $\Omega^{-1}$  at 1.8 GHz.

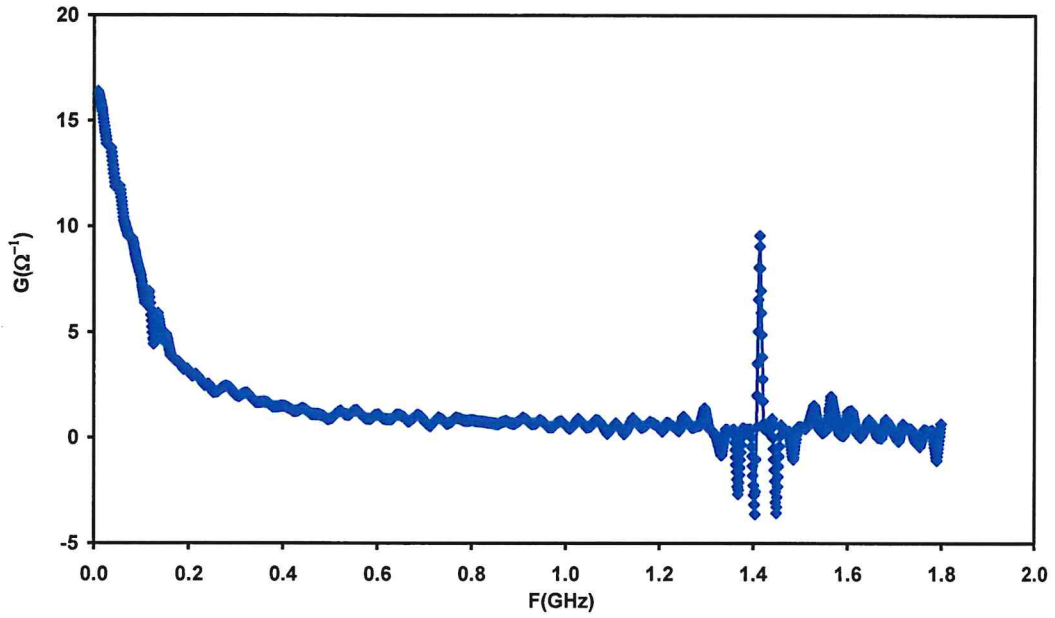


Fig 4.7: The conductance spectra for the BaSb<sub>2</sub> bulk in the frequency range (0.01-1.8) GHz.

The conductivity ( $\sigma$ ) as a function of frequency ( $\omega$ ) follows the relation  $\sigma(\omega) = A\omega^s$  [36]. Figure 4.8 represents  $\ln(G)$  versus  $\ln(\omega)$ . As  $G$  is directly proportional to  $\sigma$  we assume  $G \cong \sigma$  regardless of the dimensions of the bulk. The line fitting showed that the slope nearly is  $s = -1$ , It means that there exist a correlated barrier hopping (CBH) [36] mechanism in the samples.



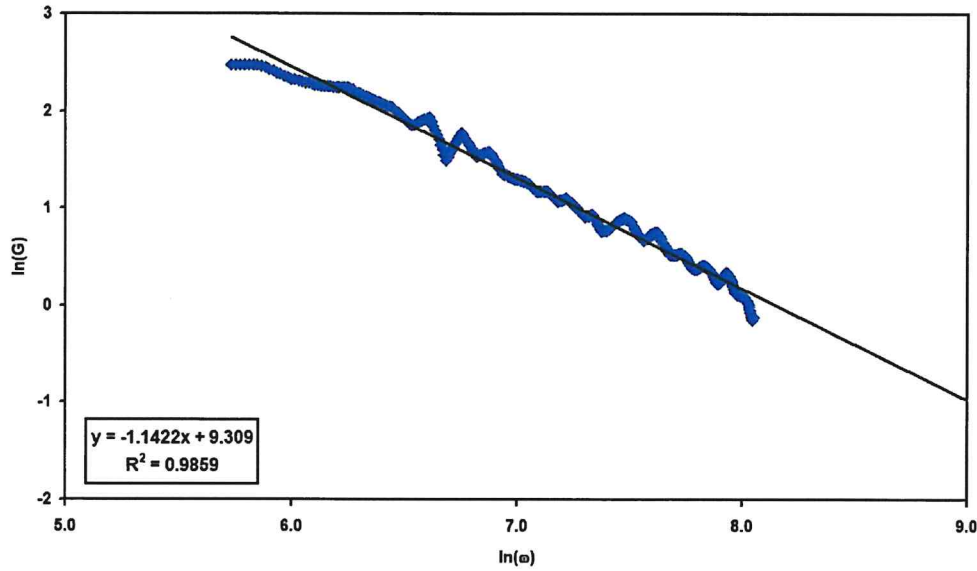


Fig 4.8:  $\ln(G)$  versus  $\ln(\omega)$  for a part of data to show the fitted line of their graph .

The conductance can be dominated by CBH, quantum mechanical tunnelling or both mechanisms. The experimental Conductance was modelled with equations 2.22, 2.28 and 2.29 as seen in figure 4.9. The good correlation between the theoretical and experimental data was achieved assuming the domination of both of QMT and CBH mechanism in the samples. The data fitting resulted in the physical parameters which are shown in table 4.7. This matching was accepted since most of the obtained data stuck in the CBH conductance and since that  $s$  value was found to be -1 as we see in figure 4.8. In accordance with the tabulated data, the scattering time ( $\tau_o$ ) is 0.17 ps which is much shorter than the hopping time ( $\tau_{hop}$ ). The phonon frequency ( $\nu$ ) was found to be 200.8  $\text{cm}^{-1}$ . The value is consistent with the assumed theoretical value 200  $\text{cm}^{-1}$  which is taken around the reported values of the phonon frequency for the Ba compounds [ 67] as 200  $\text{cm}^{-1}$ . In addition, the obtained hopping parameters presented by the density of states near



fermi level and the high and low frequency conductivities suggest that the produced BaSb<sub>2</sub> alloys are exhibiting semiconductors characteristics. Our hot probe test shows that our sample is a p-type material. The conduction type confirm the results obtained from capacitance analyses. In the c-spectra modeling we have shown the hole injection is the main reason for the apparent NC effect.

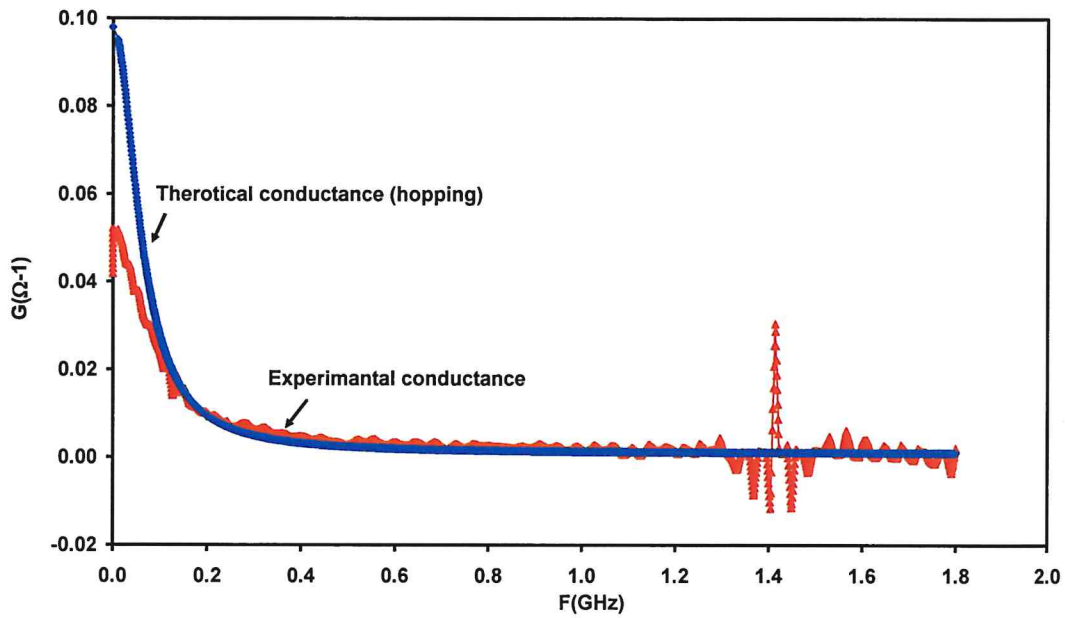


Fig 4.9: Modelling of the experimental conductance (the red line) with the theoretical or calculated one (the blue line).

As illustrated in figure 4.10, the applied AC signal showed a vibration in the impedance as the frequency increases. The vibration in the Z spectra was noticed to be increased at higher frequency nearly in the range ( 1.2-1.8 ) GHz. According to XRD analysis the prepared alloys were found to be crystalline (multistructure of monoclinic and orthorhombic), based on that result we could conclude that the vibration source is the coupling between the different layers of the BaSb<sub>2</sub> alloys which were seen in the SEM. The increased vibration in the high range of frequency may be assigned to the decrease

in the time period. Since it is inversely proportional with the frequency, so that the atoms couldn't couple in a shorter time, they try to resist that by increasing their impedance. To understand that, the impedance consists of capacitive and the resistive parts in which the total effect of them the impedance spectra represent [36]. The low impedance values at the frequencies below 1.2 GHz indicate that a high current will pass per unit voltage. These conditions have application as voltage variable capacitor [36].

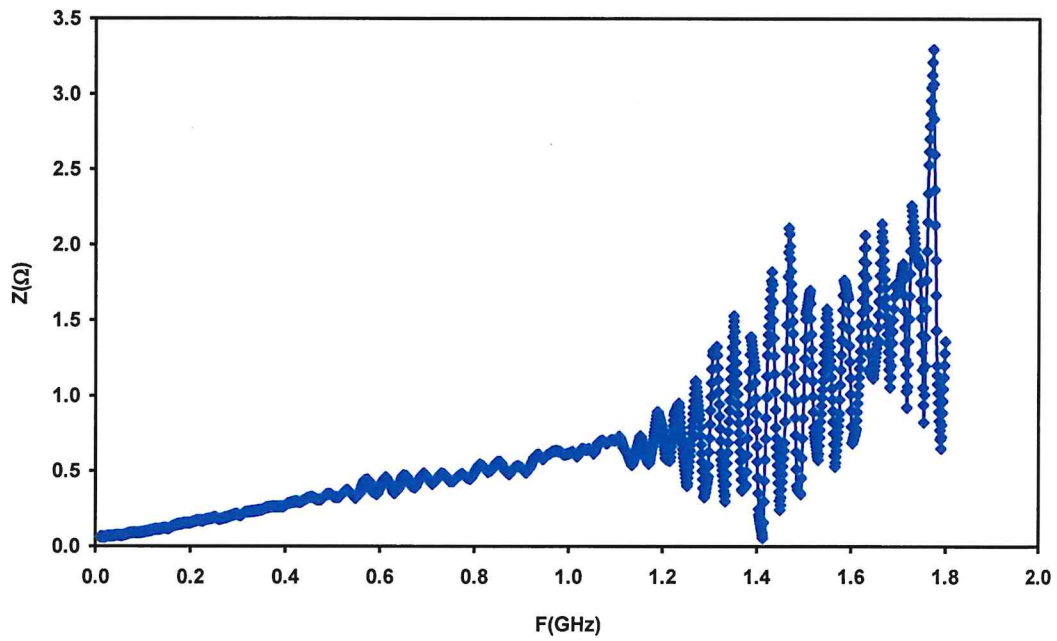


Fig 4.10: The impedance spectra for the BaSb<sub>2</sub> bulk in the frequency range (0.01-1.8)GHz.

#### 4.4 I-V Characteristics.

The I-V measurement showed that we have a linear behaviour as is shown in figure 4.11. This indicated that the prepared BaSb<sub>2</sub> alloys have an ohmic electrical property [68] . Looking again to the figure , it seems clearly that the I-V straight line nearly the same for the three respective days , these lines indicated that our material is an ordered alloys which means that the alloys contents atoms ( the Ba and the Sb atoms ) locates nearly exactly in the lattice points [69] .

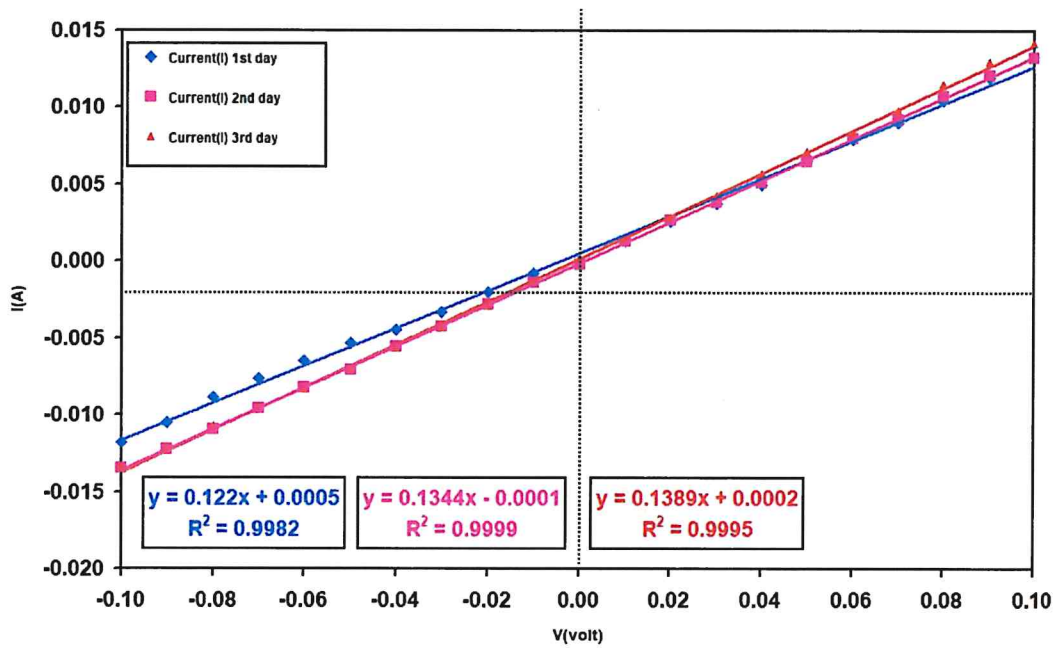


Fig 4.11: the current voltage characteristics of BaSb<sub>2</sub> alloys.

The temperature dependent resistivity measurements showed that there is a temporary metal insulator transition (MIT) . This phenomenon is provided in the theoretical part. The behaviour of MIT was present observed in Vanadium dioxide (VO<sub>2</sub>) and mentioned to

have potential applications as memory devices [70], ultrafast optical switches [71], thermochromic windows [71] and as an energy-efficient smart windows [72]. As figure 4.12 illustrates a MIT at temperature  $T_{MIT}$  nearly ( 40.5 , 73.2 , 96.6 ) K for the applied voltage values of ( 0.05, 0.02 ,0.03)Volt , respectively. In other words the MIT phenomena happened at different points for different applied voltage which provided different electric fields ( $E$ ) according to the relation  $E = V/L$ , with  $L$  being the distance between the electrodes which is 4 mm in our work . So the  $T_{MIT}$  is (40.5, 73.2, 96.6) K subjected to different fields (12.5, 5, 7.5) v/m, respectively. This variation in the temperature at which the MIT happened owing to electric field excitations is not easily interpreted. Some reasons like the degree of disorder, the band overlap, impurity concentration, etc could be suggested as we mentioned previously in chapter two [40].

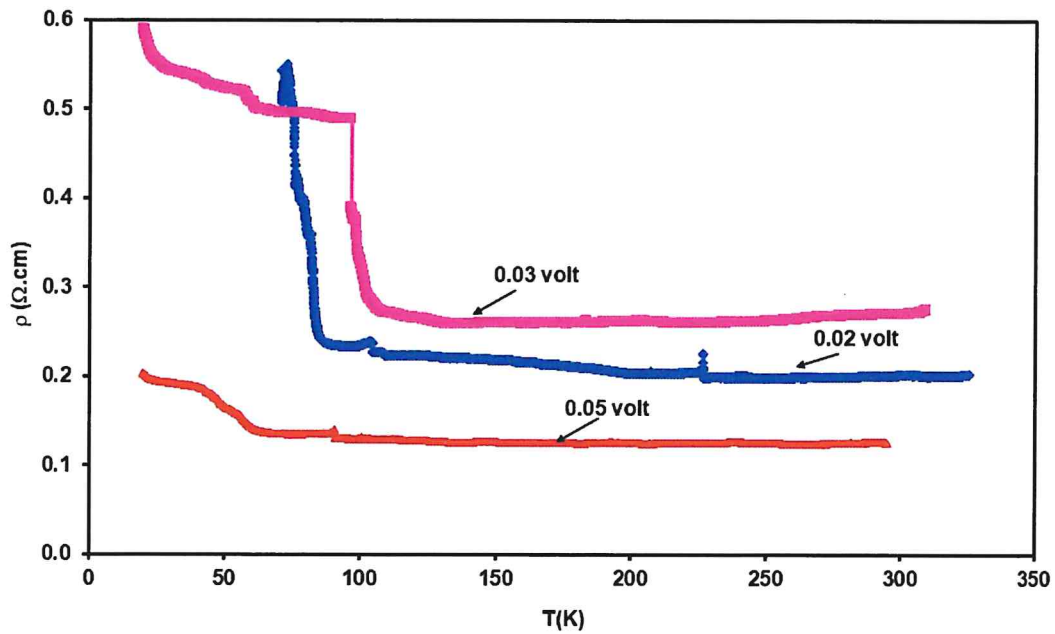


Fig 4.12: The resistivity-temperature variations of the BaSb<sub>2</sub> bulk.

## **Chapter five**

### **Conclusions**

In this thesis, we have produced new class of BaSb<sub>2</sub> alloys by the thermal evaporation of the stoichiometric metals of Sb and Ba. The alloy was studied by the x-ray diffraction, scanning electron microscopy, impedance spectroscopy and temperature dependent electrical resistivity . The main structure of the BaSb<sub>2</sub> alloys is monoclinic which also comprise other minor phases. In general, the alloys contained crystallites of sizes of 27 nm and contain low defect density. As an important class of application, BaSb<sub>2</sub> alloys exhibited negative capacitance effect over a wide range of radio and microwave frequencies. It also displays conductance spectra that could be altered with signal frequency. One important reveal about these alloys is their metal-insulator transitions. The metal insulator transitions is observed at low temperatures and is found to be highly dependent on the applied electric fields. Still the optimisation of a single structural phase of the BaSb<sub>2</sub> alloys is a challenge and need further investigations. For this reason we nominate altering the melting time and heating rates to optimise better crystalline phase of BaSb<sub>2</sub> alloys as a future work.

## References

- [1] Pearce, J. V., Edler, F., Elliott, C. J., Rosso, L., Sutton, G., Andreu, A., & Machin, G. (2017). EMPRESS: A pan-European project to enhance process efficiency through improved temperature measurement.
- [2] Duan, G., Yang, L., Liao, S., Zhang, C., Lu, X., Yang, Y., & Zhang, X. (2018). Designing for the chemical conversion coating with high corrosion resistance and low electrical contact resistance on AZ91D magnesium alloy. *Corrosion Science*, 135, 197-206.
- [3] Brif, Y., Thomas, M., & Todd, I. (2015). The use of high-entropy alloys in additive manufacturing. *Scripta Materialia*, 99, 93-96.
- [4] Palanivel, S., Kuehmann, C., Edwards, P., & Filip, E. (2019). *U.S. Patent Application No. 16/172,426*.
- [5] Abdallah, M., Kamar, E. M., Eid, S., & El-Etre, A. Y. (2016). Animal glue as green inhibitor for corrosion of aluminum and aluminum-silicon alloys in sodium hydroxide solutions. *Journal of Molecular Liquids*, 220, 755-761.
- [6] Formentini, M., & Lenci, S. (2018). An innovative building envelope (kinetic façade) with Shape Memory Alloys used as actuators and sensors. *Automation in Construction*, 85, 220-231.
- [7] Costa, J. M., de Moraes Nepel, T. C., & de Almeida Neto, A. F. (2019). Influence of current density and W concentration on Co–W alloys used as catalysts in electrodes for Li–O<sub>2</sub> batteries. *Chemical Papers*, 73(5), 1103-1112.
- [8] Gouda, E. S. (2014). Classifications, characterization and applications of metallic alloys. *International Journal of Physics and Astronomy*, 2(2), 15-49.
- [9] Palacios, T., Monge, M. A., & Pastor, J. Y. (2016). Tungsten–vanadium–yttria alloys for fusion power reactors (I): Microstructural characterization. *International Journal of Refractory Metals and Hard Materials*, 54, 433-438.
- [10] Revathy, T. A., Dhanapal, K., Dhanavel, S., Narayanan, V., & Stephen, A. (2018). Pulsed electrodeposited dendritic Pd-Ni alloy as a magnetically recoverable nanocatalyst for the hydrogenation of 4-nitrophenol. *Journal of Alloys and Compounds*, 735, 1703-1711.
- [11] He, J., Johnson, N. J., Huang, A., & Berlinguette, C. P. (2018). Electrocatalytic alloys for CO<sub>2</sub> reduction. *ChemSusChem*, 11(1), 48-57.
- [12] Liu, Y., Wang, J., Fang, Q., Liu, B., Wu, Y., & Chen, S. (2016). Preparation of superfine-grained high entropy alloy by spark plasma sintering gas atomized powder. *Intermetallics*, 68, 16-22.
- [13] Xe, L. M. (2015). Two-dimensional transition metal dichalcogenide alloys: preparation, characterization and applications. *Nanoscale*, 7(44), 18392-18401.

- [14] Kimura, T., Nakamoto, T., Ozaki, T., Sugita, K., Mizuno, M., & Araki, H. (2019). Microstructural formation and characterization mechanisms of selective laser melted Al–Si–Mg alloys with increasing magnesium content. *Materials Science and Engineering: A*, 754, 786-798.
- [15] Minciuna, M. G., Vizureanu, P., Achitei, D. C., Sandu, A. V., Berbecaru, A., & Sandu, I. G. (2016). Structural characterization and properties analysis of CoCrMoSi alloys. *Journal of optoelectronics and advanced materials*, 18(1-2), 174-178.
- [16] Shi, C., Billinge, S. J., Puma, E., Bang, S. H., Bean, N. J., de Sugny, J. C., ... & Monson, T. C. (2018). Barium titanate nanoparticles: Short-range lattice distortions with long-range cubic order. *Physical Review B*, 98(8), 085421.
- [17] Whitaker, J. C. (2018). 5.2 Power Grid Tubes. *The Electronics Handbook*, 367.
- [18] Chuntanov, K., & Setina, J. (2016). Reactive getters for MEMS applications. *Vacuum*, 123, 42-48.
- [19] Gan, C. K., & Lee, C. H. (2018). Anharmonic phonon effects on linear thermal expansion of trigonal bismuth selenide and antimony telluride crystals. *Computational Materials Science*, 151, 49-52.
- [20] Seal II, R. R., Schulz, K. J., DeYoung Jr, J. H., Sutphin, D. M., Drew, L. J., Carlin Jr, J. F., & Berger, B. R. (2017). *Antimony* (No. 1802-C). US Geological Survey.
- [21] Beswick, J., & Sherif, M. (2017). U.S. Patent No. 9,546,680. Washington, DC: U.S. Patent and Trademark Office.
- [22] Son, S. Y., Lee, D., Hur, J., & Kim, I. T. (2017). Facile synthesis of aluminum-antimony alloys and their application for lithium-ion and sodium-ion storage. *Journal of Nanoscience and Nanotechnology*, 17(10), 7575-7578.
- [23] Benchehima, M., Abid, H., Sadoun, A., & Chaouche, A. C. (2018). Optoelectronic properties of aluminum bismuth antimony ternary alloys for optical telecommunication applications: First principles calculation. *Computational Materials Science*, 155, 224-234.
- [24] Goodwin, F. E., Guruswamy, S., & Warlimont, H. (2018). Lead and Lead Alloys. In *Springer Handbook of Materials Data* (pp. 413-429). Springer, Cham.
- [25] Putero, M., Coulet, M. V., Muller, C., Baehtz, C., Raoux, S., & Cheng, H. Y. (2016). Ge-doped GaSb thin films with zero mass density change upon crystallization for applications in phase change memories. *Applied Physics Letters*, 108(10), 101909.
- [26] Luo, W., Gaumet, J. J., & Mai, L. Q. (2017). Antimony-based intermetallic compounds for lithium-ion and sodium-ion batteries: synthesis, construction and application. *Rare Metals*, 36(5), 321-338.



- [27] (Ashcroft, 1976) Neil W. Ashcroft and N. David Merman, *Solid State Physics* (Saunders College Publishing, Harcourt Brace Publishers, Fort Worth, Philadelphia, San Diego, New York, Orlando, Austin, San Antonio, Toronto, Montreal, London, Sydney, Tokyo, 1976).
- [28] Silver, Eric H. "Monochromatic X-ray methods and apparatus." U.S. Patent No. 10,299,743. 28 May 2019.
- [29] Kohli, R. (2012). Methods for monitoring and measuring cleanliness of surfaces. In *Developments in Surface Contamination and Cleaning* (pp. 107-178). William Andrew Publishing.
- [30] Kumar, Challa SSR, ed. X-ray and Neutron Techniques for Nanomaterials Characterization. Springer Berlin Heidelberg, 2015.
- [31] Ravindranadh, K., Babu, B., Rao, M. C., Shim, J., Reddy, C. V., & Ravikumar, R. V. S. S. N. (2015). Structural and photoluminescence studies of Co<sup>2+</sup> doped Ca-Li hydroxyapatite nanopowders. *Journal of Materials Science: Materials in Electronics*, 26(9), 6667-6675.
- [32] Yadav, M. R., Krishna, P. R., Rao, B. T., Rao, B. R. V., & Lakshmikanth, G. V. (2018). Influence of compositional variation on structural, optical and EPR studies of undoped and Mn<sup>2+</sup> doped lithium sodium zinc pyrophosphates (LNZP). *Materials Today: Proceedings*, 5(12), 25807-25814.
- [33] Sergey N. Makarov, Reinhold Ludwig, Stephen J. (2019) Bitar. Practical Electrical Engineering .
- [34] Al Garni, S. E., & Qasrawi, A. F. (2016). Impedance spectroscopic analysis of the InSe/ZnSe/InSe interface. *IEEE Transactions on Electron Devices*, 64(1), 244-249.
- [35] Nasri, S., Megdiche, M., & Gargouri, M. (2016). DC conductivity and study of AC electrical conduction mechanisms by non-overlapping small polaron tunneling model in LiFeP<sub>2</sub>O<sub>7</sub> ceramic. *Ceramics International*, 42(1), 943-951.
- [36] Khusayfan, N. M., Qasrawi, A. F., & Khanfar, H. K. (2018). Design and electrical performance of CdS/Sb<sub>2</sub>Te<sub>3</sub> tunneling heterojunction devices. *Materials Research Express*, 5(2), 026303.
- [37] Ghosh, A. (1990). Frequency-dependent conductivity in bismuth-vanadate glassy semiconductors. *Physical review B*, 41(3), 1479.
- [38] Ershov, M. Liu H C and Li L 1998 IEEE Transactions on Electron Devices 45 2196.
- [39] Yuan, Z. C., Rizwan, S., Wong, M., Holland, K., Anderson, S., Hook, T. B., ... & Vaidyanathan, M. (2016). Switching-speed limitations of ferroelectric negative-capacitance FETs. *IEEE Transactions on Electron Devices*, 63(10), 4046-4052.



- [40] Gantmakher, V. F., Zverev, V. N., Teplinskii, V. M., & Barkalov, I. (1993). Conduction mechanisms near the metal-insulator transition range. *Zh. Éksp. Teor. Fiz*, 103, 1460-1475.
- [41] Radisavljevic, B., & Kis, A. (2013). Mobility engineering and a metal-insulator transition in monolayer MoS<sub>2</sub>. *Nature materials*, 12(9), 815.
- [42] Chen, X., Wu, Z., Xu, S., Wang, L., Huang, R., Han, Y., ... & Wang, Y. (2015). Probing the electron states and metal-insulator transition mechanisms in molybdenum disulphide vertical heterostructures. *Nature communications*, 6, 6088.
- [43] Lee, J., Kwon, S. G., Park, J. G., & Hyeon, T. (2015). Size dependence of metal-insulator transition in stoichiometric Fe<sub>3</sub>O<sub>4</sub> nanocrystals. *Nano letters*, 15(7), 4337-4342.
- [44] Laurent, S.; Forge, D.; Port, M.; Roch, A.; Robic, C.; Vander Elst, L.; Muller, R. N. Chem. Rev. 2008, 108, 2064-2110.
- [45] Lee, N.; Hyeon, T. Chem. Soc. Rev. 2012, 41, 2575-2589.
- [46] Brito, W. H., Aguiar, M. C. O., Haule, K., & Kotliar, G. (2016). Metal-insulator transition in VO<sub>2</sub>: a DFT+ DMFT perspective. *Physical review letters*, 117(5), 056402.
- [47] Gomez-Heredia, C. L., Ramirez-Rincon, J. A., Bhardwaj, D., Rajasekar, P., Tadeo, I. J., Cervantes-Lopez, J. L., ... & Joulain, K. (2019). Measurement of the hysteretic thermal properties of W-doped and undoped nanocrystalline powders of VO<sub>2</sub>. *Scientific reports*, 9(1), 1-14.
- [48] Neil W, Ashcroft. N, Mermian. (1976).Solid State Physics ,95-97.
- [49] Eman ,Nazzal .(2017) Impact Of Indium Nano-Layers On The Physical Properties Of Ga<sub>2</sub>S<sub>3</sub> Thin Films
- [50] Reimer, Ludwig. "Scanning electron microscopy: physics of image formation and microanalysis." (2000): 1826.
- [51] Eisenmann, B., Gieck, C., & Rößler, U. (2001). Crystal structure of barium diantimonide, BaSb<sub>2</sub>. *Zeitschrift für Kristallographie-New Crystal Structures*, 216(1-4), 36-36.
- [52] Mathers, G. (2002). *The welding of aluminium and its alloys*. Woodhead publishing.
- [53] Qureshi, E. M., Shen, X., & Chang, L. (2016). An autonomous synchronized switch damping on inductance and negative capacitance for piezoelectric broadband vibration suppression. *International Journal of Aeronautical and Space Sciences*, 17(4), 501-517.
- [54] Wu, C., Zeng, S., Wang, Z., Wang, F., Zhou, H., Zhang, J., ... & Sun, L. (2018). Efficient mechanoluminescent elastomers for dual-responsive anticounterfeiting device

and stretching/strain sensor with multimode sensibility. *Advanced Functional Materials*, 28(34), 1803168.

[55] Wang, L., Tang, W., Ren, Y., Gu, J., Wang, Y., & Gu, Y. (2018, July). Improved Synchronized Switch Damping on Negative Capacitances for Semi-Active Vibration Control. In *2018 37<sup>th</sup> Chinese Control Conference (CCC)* (pp. 5064-5069). IEEE.

[56] Li, Y., Kang, Y., & Gong, X. (2017). Evaluation of negative capacitance ferroelectric MOSFET for analog circuit applications. *IEEE Transactions on Electron Devices*, 64(10), 4317-4321.

[57] Ichihara, M. (2017). *U.S. Patent No. 9,595,881*. Washington, DC: U.S. Patent and Trademark Office.

[58] Zhang, H., & Wu, A. (2018). Common-Mode Noise Reduction by Parasitic Capacitance Cancellation in the Three-Phase Inverter. *IEEE Transactions on Electromagnetic Compatibility*, 61(1), 295-300.

[59] Kjell, M. H., Jacques, E., Zenkert, D., Behm, M., & Lindbergh, G. (2011). PAN-based carbon fiber negative electrodes for structural lithium-ion batteries. *Journal of The Electrochemical Society*, 158(12), A1455-A1460.

[60] Brun, N., Prabakaran, S. R., Surcin, C., Morcrette, M., Deleuze, H., Birot, M., ... & Backov, R. (2011). Design of hierarchical porous carbonaceous foams from a dual-template approach and their use as electrochemical capacitor and Li ion battery negative electrodes. *The Journal of Physical Chemistry C*, 116(1), 1408-1421.

[61] Chen, Y., Ma, W., Cai, K., Yang, X., & Huang, C. (2017). In situ growth of polypyrrole onto three-dimensional tubular MoS<sub>2</sub> as an advanced negative electrode material for supercapacitor. *Electrochimica Acta*, 246, 615-624.

[62] Nithya, V. D., & Arul, N. S. (2016). Review on  $\alpha$ -Fe<sub>2</sub>O<sub>3</sub> based negative electrode for high performance supercapacitors. *Journal of Power Sources*, 327, 297-318.

[63] Sharma, P., Zhang, J., Ni, K., & Datta, S. (2017). Time-resolved measurement of negative capacitance. *IEEE Electron Device Letters*, 39(2), 272-275.

[64] Qiu, C., Liu, F., Xu, L., Deng, B., Xiao, M., Si, J., ... & Peng, H. (2018). Dirac-source field-effect transistors as energy-efficient, high-performance electronic switches. *Science*, 361(6400), 387-392.

[65] Bisquert, J., Garcia-Belmonte, G., Pitarch, Á., & Bolink, H. J. (2006). Negative capacitance caused by electron injection through interfacial states in organic light-emitting diodes. *Chemical Physics Letters*, 422(1-3), 184-191.

[66] Catalan, G., Jiménez, D., & Gruverman, A. (2015). Ferroelectrics: Negative capacitance detected. *Nature materials*, 14(2), 137.

- [67] Pfau, C., Miclea, P. T., Bohley, C., & Schweizer, S. (2010). Phonon spectra of barium halide nanocrystals in fluorozirconate glasses. In *IOP Conference Series: Materials Science and Engineering* (Vol. 15, No. 1, p. 012021). IOP Publishing.
- [68] Ghahfarokhi, P. S., Kallaste, A., Belahcen, A., & Vaimann, T. (2016, May). Thermal analysis of electromagnetic levitation coil. In *2016 17th International Scientific Conference on Electric Power Engineering (EPE)* (pp. 1-5). IEEE.
- [69] Kittel, C., McEuen, P., & McEuen, P. (1996). *Introduction to solid state physics* (Vol. 8, pp. 105-130). New York: Wiley.
- [70] Fan, L., Chen, Y., Liu, Q., Chen, S., Zhu, L., Meng, Q., ... & Zou, C. (2016). Infrared response and optoelectronic memory device fabrication based on epitaxial VO<sub>2</sub> film. *ACS applied materials & interfaces*, 8(48), 32971-32977.
- [71] Majid, S. S., Gautam, K., Ahad, A., Rahman, F., Choudhary, R. J., De Groot, F. M., & Shukla, D. K. (2019). Mott-Hubbard insulator-metal transition in the VO<sub>2</sub> thin film: A combined XAS and resonant PES study. *arXiv preprint arXiv:1907.12746*.
- [72] Ren, H., Li, B., Zhou, X., Chen, S., Li, Y., Hu, C., ... & Zou, C. (2019). Wafer-size VO<sub>2</sub> film prepared by facile water-vapor assisted thermal oxidation of metallic vanadium film. *arXiv preprint arXiv:1910.08776*.

### الملخص

في هذه الرسالة ، تم إنتاج سبائك  $BaSb_2$  و دراستها. تم فحص السبائك التي تم تحضيرها بواسطة تذييب Ba و Sb في تكوين كيميائي متوازن في وسط فراغ قيمته  $10^{-5}$  ميلي بار عند درجة حرارة 735 درجة مئوية بنائياً وكهربائياً. أثبتت الابحاث الهيكلية العميقة بمساعدة حزم حيود الأشعة السينية و البرامج "Crystdiff" و "Treor 92" و "phywe measure 4" أن السبائك تتكون من بناء المونوكلينيك (58.46%) و ابنية ثانوية اخرى (41.54%). أشارت المعاملات الهيكلية إلى أن السبائك تتكون من بلورات نانو وتظهر نسبة منخفضة من التراص وكثافة عيوب منخفضة. أظهرت تحاليل المورفولوجيا التي تم إجراؤها باستخدام الفحص المجهرى الإلكتروني للمسح أن السبائك هي من الأنواع التي تكون على شكل طبقات وتحتوي على شقوق ضيقة بطول 5.0 ميكرومتر. كهربائياً السبائك المعدنية هي مواد من نوع p التي تظهر تحولات معدن عازل في درجات حرارة منخفضة. تعتمد درجة الحرارة الانتقالية بدرجة كبيرة على المجال الكهربائي المؤثر . أظهر تحليل التيار المتردد على أطيف السعة والتوصيل التي تم قياسها في مجال التردد البالغ (0.01-1.8) غيغاهرتز أن السعة تظهر تأثير السعة السلبي بسبب حقن هولات أكبر من اللإلكترونات . بالإضافة إلى ذلك ، أظهرت نمذجة أطيف التوصيل في مجال التردد الرئيسي أن سبائك  $BaSb_2$  يسيطر عليها توصيل الهوبينج في أوقات تشتت بالبيكو ثانية. ترشح الخواص الكهربائية لسبائك  $BaSb_2$  لاستخدامها في الدوائر لاغية للسعة وكمخفضات للضوضاء.